ISAS - INTERNATIONAL SCHOOL FOR ADVANCED STUDIES

Scuola Internazionale Superiore di Studi Avanzati

International School for Advanced Studies

Conformational Substate Distribution in high spin ferric Myoglobin as studied by Electron Paramagnetic Resonance

Thesis submitted for Degree of

"Doctor Philosophiæ"

CANDIDATE

Anna Rita Bizzarri

SUPERVISOR

Prof. Salvatore Cannistraro

a.a. 1990–91

TRIESTE

SISSA - SCUOLA INTERNAZIONALE SUPERIORE DI STUDI AVANZATI

TRIESTE

Strada Costiera 11

Scuola Internazionale Superiore di Studi Avanzati

International School for Advanced Studies

Conformational Substate Distribution in high spin ferric Myoglobin as studied by Electron Paramagnetic Resonance

Thesis submitted for Degree of

"Doctor Philosophiæ"

CANDIDATE

Anna Rita Bizzarri

SUPERVISOR

Prof. Salvatore Cannistraro

a.a. 1990–91

NOTES

Part of this thesis has been published and presented to congresses.

Pubblications

–"Solvent Effects on Myoglobin Conformational Substates as studied by Electron Paramagnetic Resonance."

A.R. Bizzarri and S. Cannistraro, Biophys. Chem. (1991) in press.

–"An Electron Paramagnetic Resonance study of Conformational Substates distribution in high spin Heme–proteins."

A.R. Bizzarri and S. Cannistraro, submitted to Appl. Magn. Res.

Contributions to Conferences

–"Conformational substates and distribution of spin hamiltonian parameters."

A.R. Bizzarri and S. Cannistraro Congresso Nazionale di Risonanze Magnetiche -Pisa Ottobre 1990.

–"Studio mediante EPR di sottostati conformazionali in emo proteine."

A.R. Bizzarri and S. Cannistraro Congresso Nazionale di Risonanze Magnetiche -Milano Ottobre 1991.

Contents

Introduction

Proteins are dynamical objects which can assume different functional states; each of them being characterized by a very large number of nearly isoenergetic conformational substates (CS) [1,2] that may be modulated by external agents such as pressure, pH and solvent [3–5]. Sampling of CS is relevant to the biological functionality of proteins, since molecules encompass a wide range of structures which perform the same function but with different rates [6]. At room temperature, a protein molecule moves from one substate to another, with rates depending on both the protein structure and the medium in which the molecule is embedded [4] [7–9]. By decreasing temperature, a protein solution undergoes a glass–like transition and biomolecules may be frozen in many different CS whose distribution is connected with the dynamic properties of the protein–solvent system at physiological temperatures [10].

Myoglobin (Mb), one of the most studied proteins, represents a sort of guide to investigate the relationship among the presence of CS distribution, dynamics and functionality. At present, most of this information comes from optical spectroscopic studies on the CO rebinding kinetics performed on Mb solutions at different temperatures [1,4]. However, for this kind of studies the samples must be transparent and such a goal is currently achieved by adding more than 50% by volume of either glycerol or ethylene glycol to protein aqueous solutions.

Quite recently, electron paramagnetic resonance (EPR) spectroscopy has been revealed to be a promising tool to investigate the CS distribution in

metallo–proteins [11,12]. The underlying idea is that the presence of a CS distribution entails a distribution of some of the metal ion crystal field parameters and, consequently, characteristic features appear in the spectra. Therefore, EPR, which does not require any added solvent and, at the same time, can be performed in the presence of different solvents, results particularly suitable to the study of the connection between CS distribution and dynamics of the protein–solvent system.

In the present work, EPR spectroscopy has been applied to investigate the presence of CS in Mb. In particular, the possible mechanisms involved in the coupling among solvent, CS distribution and the arrangement of the metal ion in the heme–group have been analyzed in detail.

The thesis is organized as follows. In Chapter 1, an introduction to CS in proteins, and in particular in Mb, is presented. Some implications of the presence of CS distribution for protein dynamics, and the connections with the behaviour of other complex systems, are briefly discussed.

The general principles of EPR spectroscopy and the experimental apparatus are briefly reviewed in Chapter 2. Moreover, the electronic structure of the ferric ion in the cubic ligand field of the heme–group with some details concerning the high spin configuration, particularly relevant for our analysis, are therein discussed. Finally, the simulation method employed to analyze the EPR spectra of high spin ferric heme–proteins is reported.

In Chapter 3, the EPR spectra of high spin ferric Mb at different conditions are carefully analyzed in terms of the distributions of two metal ion crystal field parameters. These distributions are shown to be dependent on i) the solvent used; ii) the pH of the solutions and iii) the cooling rate to which the samples were submitted. The connection between the widths of these distributions and

the CS distribution is discussed.

In Chapter 4, the crystal field parameter distributions have been interpreted, by an approach based on the angular overlap method (AOM), in terms of distributions of some parameters characterizing the heme–group. In particular, it has been shown that the iron–porphyrin displacement is distributed as consequence of the presence of CS distribution.

Finally, in Conclusions, some notes concerning the applicability of EPR spectroscopy to extract information about CS distribution in Mb samples, are briefly presented.

Chapter 1

Proteins dynamics: an approach based on the CS distribution

1.1 Proteins : structure, dynamics and functionality

Proteins, essential components of all living organisms, are responsible for a wide range of biological functions. An important characteristic of proteins is their specificity; it can be found a very large number of different protein molecules, each one built to perform a very particular function.

Proteins are large molecules whose basic component is the polypeptide chain, an unbranched polymer consisting of a sequence of amino–acid residues, complemented, in some cases, by one or more prosthetic groups. The polypeptide chain of globular proteins is folded, in water, compactly into a characteristic three dimensional structure. Different kinds of interactions, between protein–protein, protein–solvent, solvent–solvent, stabilize the protein structure.

The biological functionality of proteins, in many cases, requires the presence at least of two different states; the passage from one state to another can involve deep changes in the overall protein structure.

5 PROTEINS DYNAMICS

Covalent and non–covalent bonds, in proteins, are permissive of different types of internal motions that cover a large range in magnitude (from hundredths of an angstrom to tens of angstroms), and an enormous range in time (from sub–picoseconds to seconds). Some of these motions are known to have a functional role since they are involved into the passage from one state to another state.
In order to interpret internal motions of proteins within each state, two basic models have been proposed. The first model assumes that the atomic motions arise from harmonic vibrations within a single multidimensional potential [13,14]; the second model is based on a multiminimum surface where the motions are superposition of oscillations within a well and transitions among different wells [6,15]. In the last model, the protein can assume a very large number of substates called conformational substates (CS), which differ among them for what concerns structural details. The last model has been supported by different kinds of analysis, for example, X–ray diffraction [16], Mössbauer spectroscopy [17], inelastic neutron scattering [18,19], flash photolysis experiments [6], molecular dynamics simulations [15]; from these analyses, it comes out that the side chains of amino–acids and the hydrogen bonds in proteins can assume a variety of slightly different positions.
These CS are assumed to have, at physiological temperature, a biological role; in fact, molecules in different substates perform the same function but possibly with different rates [6]. Moreover, the coupling (through the fluctuation–dissipation theorem [20]), between the *equilibrium fluctuations*, which characterize a protein molecule in equilibrium at high temperature, and the so called *functionally important motions*, related to transitions from one state to another one, causes dynamics and functionality to be strictly correlated.

1.2 Proteins as complex systems

Proteins show a close similarity with other complex systems like glasses [21,22], spin glasses [23,24], neural networks [25].

Complexity, in natural systems, typically arises from the collective effect of a large number of simple components. Moreover, systems consisting of simple parts behave with a degree of complexity which is intimately related to the diversity of the interactions present in the systems [26,27]. The presence of many amino–acid residues and the high degree of interaction diversity among these residues could be assumed to cause the complex behaviour of protein systems. As it is known, a typical characteristic of many complex systems is the metastability, *i.e.* the existence of many nearly isoenergetic ground states; in this context, the presence of many CS, in proteins, could be seen as a consequence of the complex character of the system.

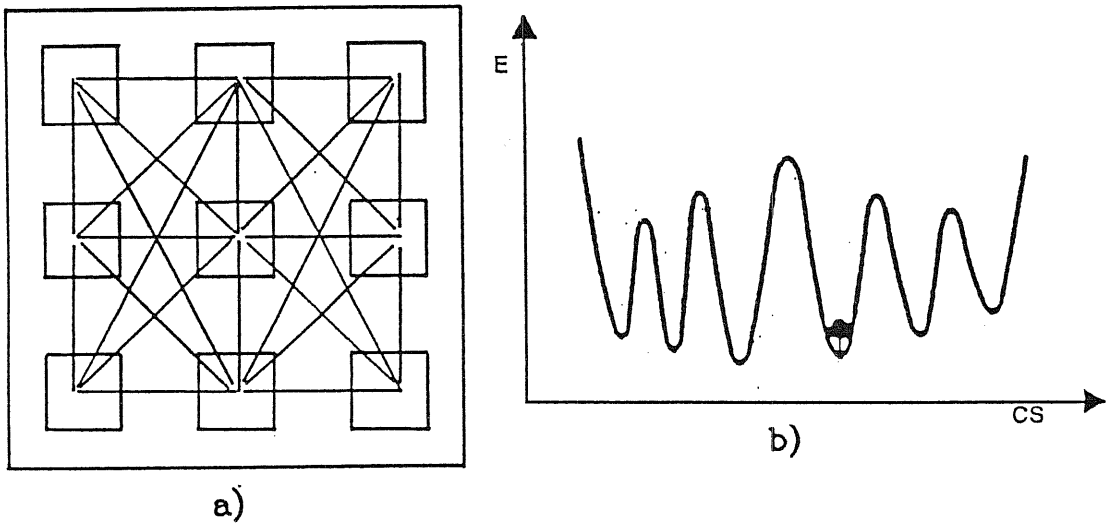

Figure 1.1. Complexity. a) A schematic figure of a generic system built by different simple parts mutually interacting is shown. b) The presence of many nearly isoenergetic states characterizes complex systems (metastability).

It has been hypothesized that CS could play a relevant role in the protein

folding. In particular, the presence of many metastable states would imply a multiplicity of pathways for the folding process [28]. Then, the existence of CS might render feasible the real folding of proteins.

In analogy with the behaviour of complex systems in general, it has been supposed that CS could be arranged in a hierarchical way. Some experimental evidences seem to point out that a sort of hierarchical arrangement of the CS in proteins could be present [6].

Concerning dynamics, it should be noted that in general it is extremely hard to to simulate on a computer the dynamical behaviour of complex systems. It has been suggested that the reason might be that many complex systems actually function as computers, performing computations which cannot be completed in fewer logical steps than the systems are using themselves [29]. In this context, it can be observed that a direct solution of problems concerning protein dynamics is quite difficult to be reached by means of traditional computational methods.

1.2.1 Proteins and glasses

At low temperature, the fluctuations among CS can be suppressed and the protein solution undergoes a glass–like transition below which the protein molecules are frozen in many CS. On the other hand, it has been observed that proteins show a glass–like behaviour for what concerns different properties; for example, the response to some perturbations can be described by α–relaxation [22,30] characterized by a nonexponential time dependence and a non–Arrhenius temperature dependence. Moreover, proteins and glasses share characteristic anomalies in their thermal, dielectric and electron paramagnetic properties [31,32] [33,34]. In particular, low temperature thermal and dielectric properties

of proteins show low energy excitations similar to those found in glasses [33], their anomalies in the vibrational states having being described in the framework of the two level tunneling system model [31,33]. EPR spectra of some copper proteins and of some Cu^{2+}–doped glasses formed by water and a second component show that these systems are characterized by a distribution of ligand field strengths onto the metal ion; such a distribution has been put into relation to the distribution of the CS energies in both the metallo–proteins and the amorphous matrices [35].

Actually, the glass–like transition in proteins is indicated as "slaved " to the solvent, since the corresponding glass–temperature, T_f, markedly depends on the solvent [7]; consequently, the CS distribution could be strongly affected by the solvent composition. In this context, it has been suggested that the glass–like behaviour of proteins could be due to randomized local arrangement [21,23] [36,37] of certain atoms or group of atoms and that hydration water could play a crucial role in the dynamical arrest of the CS [31,36] [38,39]. Therefore, the solvent could act on the protein dynamics both by affecting the transitions among CS and by modifying the intrinsic CS distribution.

1.3 Myoglobin and CS distribution

Myoglobin (Mb) is one of the most studied proteins and it represents a sort of guide into the study of CS. Different kinds of approaches have been performed in Mb samples in order to investigate both the properties of the CS distribution, and the effects of these CS on the biological functionality of the protein [1].

The existence of many different CS in Mb samples has been verified by different experimental techniques; X–ray diffraction [16,40], inelastic neutron scattering

[18], Mössbauer spectroscopy [2,17] flash photolysis experiments [6,30], and also by molecular dynamics simulations [15,41].

The application of X-ray diffraction and of flash photolysis to Mb will be briefly described since they have some relevance for our results.

1.3.1 Myoglobin structure

Mb, a globular protein found in skeletal and heart muscle where it functions to store and to transport molecular oxygen, has an extremely compact structure whose dimensions are of about 45 × 35 × 25 Å. It was the first protein for which a complete three dimensional structure was determined [42]. Mb is built of a single chain of 153 amino–acid residues, organized for 75% into helical regions, and of a non covalently bond protoporphyrin IX heme prosthetic group.

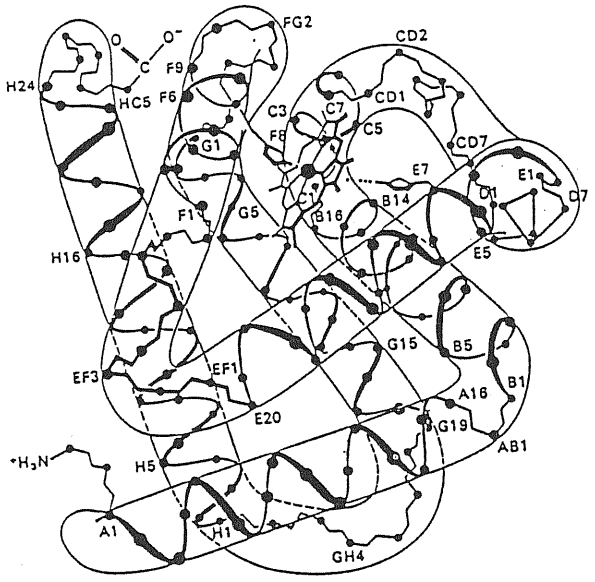

Figure 1.2. It is shown a model of Mb at high resolution with only α–carbons and the heme group drawn. From ref. [43].

On one side of the heme plane, the iron is directly bound to an azote atom of the imidazole of a histidine residue, called proximal histidine (F8), while on the

other side, at which the distal histidine residue (E7) is placed, the iron can bind the molecular oxygen (or in some case other ligands like CO). Some controls for the binding steps come from the proximal side through the protein structure [44].

In the deoxy structure, the metal ion is about $0.5\mathring{A}$ out of the heme–plane which has a domed structure; while in the bound state, the iron is found closer to the heme plane which has, on the contrary, a quite planar structure.

1.3.2 X-ray diffraction

X-ray diffraction, which can be employed to determine, at a high level of resolution, the three dimensional structure of proteins, can be also applied to extract information about other aspects of macromolecules.

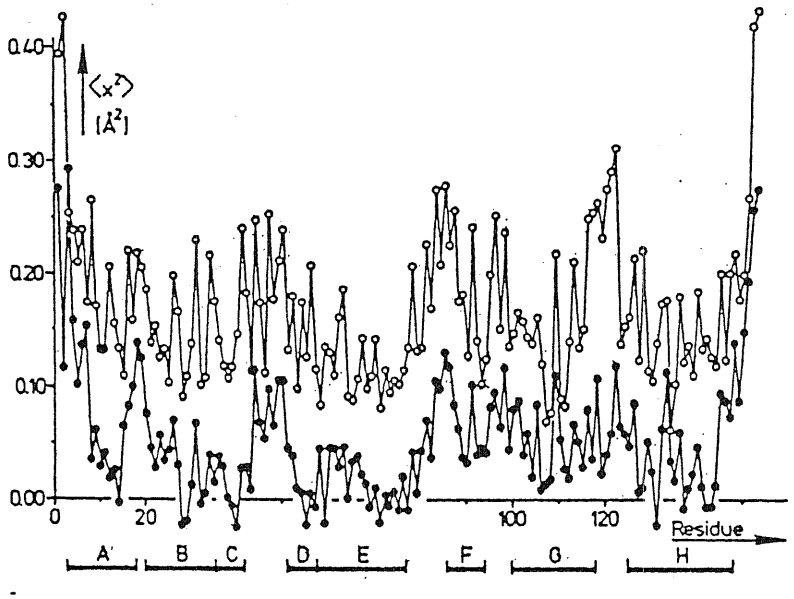

Figure 1.3. Mean square displacements of the side–chain atoms of metMb; open circles: interpolation to 300 K; full circles: linear extrapolation to 0 K. From ref. [40].

The mean–square displacements $< x^2 >$ for the individual atoms in a protein

crystal include different contributes: vibrations, lattice disorder, rotational and translational diffusion, and possibly the contributes arising from the presence of a CS distribution [16]. An analysis of the behaviour, at different temperatures, of $< x^2 >$ for the backbone and side–chain atoms, has led to determine, in Mb, the presence of an intrinsic structural disorder in agreement with the existence of many different CS [16,40]. In particular, the side chains of the amino–acids can be arranged in slightly different positions.

1.3.3 Flash photolysis experiments

One of the most representative experimental evidences for CS is given by the CO–rebinding kinetics studies performed on Mb solution composed by water and a second component, usually, glycerol or ethylene glycol [1,4]. Mb molecules are initially in the bound state in which the ligand (CO) is linked to the heme iron. A light pulse breaks the iron–ligand bond and the ligand passes to the heme pocket, and subsequently, if the temperature is sufficiently low, it rebinds to iron. At higher temperatures, the ligand, in the heme–pocket, may escape into the solvent and additional processes should be taken into account [30]. Generally, the temperature at which the escape begins depends on the composition of the solvent in which the protein is embedded; for water–glycerol (75%) solutions, the temperature–escape is about 180 K. Rebinding kinetics, monitored at different bands (Soret, near infrared, infrared) have been followed at different temperatures [6,10].

The survival probability, *i.e.* the fraction of Mb molecules that have not rebound the ligand at the time t after photodissociation, shows a non–exponential time course for $T < 180\ K$. This behaviour has been explained by assuming

that proteins are inhomogeneous, this means that each molecule responds in a slightly different way to the rebinding process. It has been supposed that the activation enthalpy barrier H, related to the CO rebinding from the heme pocket, may assume different values. In this context, the survival probability N(t) can be expressed by

$$N(t) = \int g(H) e^{-k(H)t} dH \tag{1}$$

where g(H) is the density probability for the activation enthalpy, k(H) is the rate constant which is given the Arrhenius relation

$$k(H) = Ae^{-\frac{H}{kT}} \tag{2}$$

From the experimental data for N(t), by a Laplace inversion, g(H) can be derived [45]. Therefore, the presence of CS distribution to which such a heterogeneity in the protein ensemble should be attributed, results in a distribution of a parameter (the activation H) directly involved in the biological functionality. Different approaches have been developed in order to build a model for such a process and to derive some analytical expressions for g(H) [46–48].

Chapter 2

Application of EPR spectroscopy to the study of ferric myoglobin

2.1 General principles of the EPR spectroscopy

Electron Paramagnetic Resonance (EPR) spectroscopy is a technique that detects unpaired electrons by absorption of energy from microwave irradiation when the sample is placed in a static magnetic field [49]. The magnetic moment of the electron, resulting from the intrinsic spin (S=1/2), in presence of a static magnetic field has two orientations with different energies. Transitions between the two spin states can be induced if an oscillating electromagnetic radiation of appropriate frequency ν is applied perpendicular to the external magnetic field H. The basic resonance condition is expressed by

$$h\nu = g\beta H \tag{3}$$

where h is the Planck constant ($h = 6.62510^{-27} erg\ sec$), β is the Bohr magneton ($\beta = 9.27\ 10^{-21}\ erg\ G^{-1}$), g is the electron g–factor which for free electrons is 2.0023. Local internal field, induced by the external field, can cause the value of g, for an unpaired electron in a molecule, to vary from the value for

the free electron. Moreover, the value of g generally vary with respect to the orientation of the molecule relative to the magnetic field (g–anisotropy) and, in general, g must be expressed as a tensor.

Let us consider a system , in a static magnetic field, with two spin states, if N_A is the number of spins in the lowest state (A) with energy E_A, and N_B the number in the upper one (B) with energy E_B, at the thermal equilibrium, from the Boltzmann's law, it follows

$$\frac{N_A}{N_B} = e^{\frac{E_B - E_A}{kT}} \tag{4}$$

$E_B - E_A$, the energy difference between the two spin states, is equal to $g\beta H$. From eq.(4), it results that $N_A \neq N_B$ and then the system has a net magnetic moment along the direction of the magnetic field. The magnetization for unit volume is given by

$$M = \frac{N_A - N_B}{V}\mu \tag{5}$$

where μ is the magnetic moment of each dipole and V the volume of the sample. The transition probability from the A state to the B state, induced by an oscillating magnetic field $\mathbf{H_1}(t)$ perpendicular to the static magnetic field, can be described by the time–dependent perturbation theory and it is given by

$$P_{AB} = \frac{4\pi^2}{h} |< B \mid \mathbf{H_1}(t) \mid A >|^2 \, \delta(E_B - E_A - h\nu) \tag{6}$$

where $\mathbf{H_1}(t)$ is the time–dependent perturbation, δ is the Dirac function, and ν is the frequency of the electromagnetic radiation. Moreover, it results that $P_{AB} = P_{BA} = P$, i.e. the upward and the downward transition probability are equal. The introduction of the δ–function in eq.(6) means that the quantum energy $h\nu$ of radiation should be exactly equal to the energy difference between the states. In reality, different processes contribute to produce the width and

the shape of the resonance absorption line. First of all, the existence of relaxation processes, which cause a finite lifetime of the spin states, contributes to a broadening of the linewidth.

A phenomenological description of the resonance, characterized by the longitudinal relaxation time T_1 and by the transversal relaxation time T_2', can be done by means of the Block equations (see for example [43,50]). In such an approach, the time evolution for the magnetization is given by

$$\frac{d\mathbf{M}}{dt} = \mathbf{M} \cdot \gamma \mathbf{H} \tag{7}$$

$\mathbf{H} = \mathbf{H_o} + \mathbf{H_1}$, where $\mathbf{H_o}$ is the static magnetic field assumed along the z axis and $\mathbf{H_1}$ is the oscillating magnetic field which is assumed bolonging to the xy plane. In the assumption that any deviation from the equilibrium value M_z^o, of the z component of $\mathbf{M}$, would result in a first order relaxation back to equilibrium, and that any deviation of M_x and M_y from zero will tend to relax toward zero in a first order fashion, the eq.(7) becomes

$$\frac{dM_x}{dt} = \gamma M_y H_o + \gamma M_z H_1 sin(\omega t) - \left[\frac{M_x}{T_2'}\right] \tag{8}$$

$$\frac{dM_y}{dt} = -\gamma M_x H_o + \gamma M_z H_1 cos(\omega t) - \left[\frac{M_y}{T_2'}\right] \tag{9}$$

$$\frac{dM_z}{dt} = -\gamma M_x H_1 sin(\omega t) - \gamma M_y H_1 cos(\omega t) - \left[\frac{M_z - M_z^o)}{T_1}\right] \tag{10}$$

By solving the Block eqs.(8–10), it can be shown that [50] that the average rate A at which energy is absorbed, per unit of volume, by the sample from the $\mathbf{H_1}$ field, depends on the out–of–phase component of the magnetization. In particular, it is

$$A = 2\omega\chi'' H_1^2 \tag{11}$$

where χ'' is the imaginary part of the susceptibility.

T_1 is a measure of the time, for the spin system, to approach the thermal equilibrium after the turning on of the static magnetic field, and it can be expressed by

$$T_1 = \frac{1}{W_{AB} + W_{BA}} \tag{12}$$

where W_{AB} and W_{BA} are the upward and downward transition relaxation probabilities between the A and B states, respectively. In the relaxation process associated to T_1, called spin–lattice relaxation, magnetic moments give up energy to the lattice; this phenomenon is possible since the spin system is coupled to the thermal motions of the lattice (gas, liquid or solid).

T_2' describes the spin–spin relaxation process. The presence of this relaxation process, due to the interaction between the dipoles, causes fluctuations of the energy levels, and it is responsible for the loss of spin coherence and for the observed vanishing of the transverse component in resonance phenomena.

Relaxation processes lead to a homogeneous line broadening, this means that the average magnetic field at each dipole can be considered the same (also if the instantaneous magnetic field can be different for each dipole). A parameter T_2 which encompasses both the two lifetime broadening can be expressed by

$$\frac{1}{T_2} = \frac{1}{T_2'} + \frac{1}{2T_1} \tag{13}$$

In the absence of other broadening mechanisms, T_2 is the width of half height of the absorption signal.

For most transition metal ions, relaxation processes are governed exclusively by their small values of T_1, and since the rise in temperature results in a rapid increase of the rate at which transitions between the various vibronic levels are induced by the phonon system, lines broadened as consequence of these phenomena can be sharpened by lowering the temperature of the sample.Then, low temperature is required to visualize the absorption resonance lines.

If we call n the difference between the two spin states N_A and N_B, ($n = N_A - N_B$), the rate of change of population, in the presence of electromagnetic radiation and relaxation processes, can be expressed by

$$\frac{dn}{dt} = -2Pn - \frac{n - n_o}{T_1} \tag{14}$$

where n_o is the n-value at the thermal equilibrium.

It can be shown that at opportune powers, in order to satisfy the condition $PT_1 \ll 1$, saturation could be avoided and the resonance absorption line can be detected.

Homogeneous line broadening, in many cases, can be satisfactory represented by a Lorentzian lineshape. Actually, to reproduce the observed linewidth, additional broadening mechanisms, strictly depending on the analyzed system, should be introduced. These additional effects which are operative in determining the EPR spectra of heme–proteins, will be analyzed afterwards.

2.1.1 Basis of the experimental detection of resonance

Microwave power absorption of paramagnetic samples can be detected in opportune conditions. In general, it is required a source of a variable magnetic field, a source of radiation in the microwave region and some means of detecting absorption of the sample. A typical spectrometer has been schematized in Fig.2.1.

The sample is placed into the resonance cavity which, on turn, is put in the static magnetic field. The static magnetic field, generated by an electromagnet, should be stable and uniform over the sample volume; stability is checked by means of a feed–back circuit, which usually employs a Hall–effect devise, detecting directly any deviation of the magnetic field. The microwaves, generated by a

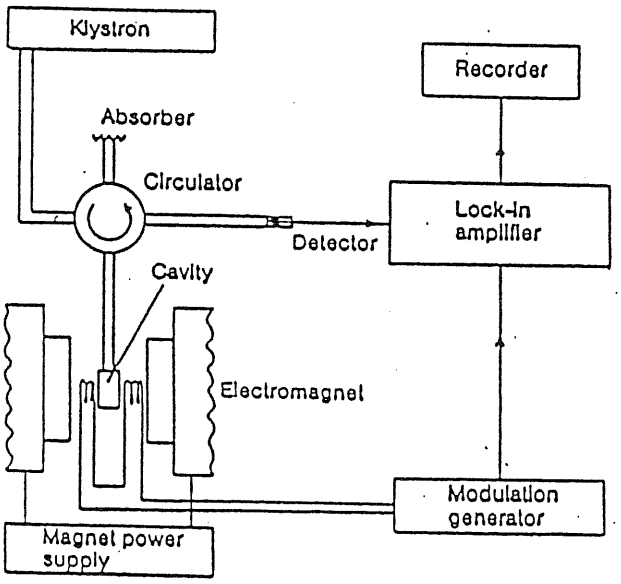

Figure 2.1. Block diagram of an EPR spectrometer.

klystron, centered on a small range of frequency (for the X-band, this range is of 8.2 to 12.4 GHz), are transmitted, eventually attenuated, down the cavity. In order to scan the resonance, for which $h\nu = g\beta H$, the magnetic field is swept linearly while the klystron frequency is held fixed at the resonance frequency of the cavity.

The use of a resonance cavity allows us to increase the density of the electromagnetic energy in the sample, and then the sensitivity of the detection. The ability of the cavity to concentrate power is measured by the Q–factor which is defined as

$$Q = 2\pi \frac{energy\ stored\ in\ the\ cavity}{energy\ dissipated\ per\ cycle} \tag{15}$$

Different geometrical forms for cavities can be employed, the most common are the rectangular with mode T_{102} and the cylindrical with mode T_{011}.

In general, the resonance cavity may be represented by the impedance Z, with R, L and C the equivalent resistance, inductance and capacity of the cavity

$$Z = R + j(\omega L - \frac{1}{\omega C}) \tag{16}$$

L is given by

$$L = L_o(1 + 4\pi\xi\chi) \tag{17}$$

where L_o is the inductance when the sample is off magnetic resonance; ξ is the filling factor ($0 < \xi < 1$); and χ is the complex susceptibility.

The resistive component of the cavity impedance is tuned to the impedance of the transmittion line in such a way that reflection of microwave energy from the cavity is minimized. At the resonance, the variation of the cavity Q–value that accounts for absorption of power from the sample is

$$dQ = -Q^2 4\pi\xi\chi'' \tag{18}$$

where χ'' is the imaginary part of the susceptibility of the sample.

The detection system is built, by means of the four–port microwave circulator, to pick up only the unbalanced microwave power produced when the condition of resonance is fulfilled. The employment of this four–port microwave circulator permits to reach a high sensitivity for the detection. The detector, a silicon crystal, put at the end of one of the arms of the circulator, is chosen in such a way that the crystal current is proportional to the microwave power falling on it.

In order to limit noise from crystal detector and from the klystron, a small–amplitude magnetic field, commonly at 100 kHz, is superimposed upon the static magnetic field. The signal can be amplified by a lock–in amplifier and then registered on a chart recorder. Because of the modulation, the recorded spectrum gives the first derivative of the microwave power absorption with respect to the magnetic field.

2.2 Electronic structure of ferric ion

Let us consider heme–proteins in which the heme prosthetic group includes the iron, a paramagnetic element of the first transition series. The presence of the incomplete d–shell is responsible, in the neutral or ionic states (Fe^{2+} and Fe^{3+}), for the paramagnetic properties of this element. The ferric ion (Fe^{3+}) has 23 electrons arranged in the electronic configuration $(3d)^5$. In an isolated ion, the five d orbitals have the same energy and the ground state is represented, in accordance with the Hund rule, by the sextet (^6S) corresponding to the highest multiplicity. In general, the electronic configuration d^5 gives rise to 16 terms which can be formed into three different groups, each one with an assigned spin state; in the Russell–Saunders representation (S,L), they could be expressed by

$$S = \frac{5}{2} \qquad {}^6S$$

$$S = \frac{3}{2} \qquad {}^4P, {}^4D, {}^4F, {}^4G$$

$$S = \frac{1}{2} \qquad {}^2S, {}^2P, {}^2D, {}^2F, {}^2G, {}^2H, {}^2I$$

Energy separations between these (S,L) terms, as due to interelectronic Coulomb repulsion, can be expressed in terms of the Racah parameters B and C [51].

Transition elements can form complexes (called also coordination compounds) characterized by a cluster of ions or molecules (ligands) surrounding the metal ion. The perturbations exerted by the ligands on the ion can greatly affect the energy of its d–orbitals, which can result to be split. The separation among the d–orbitals can be described by different approaches, for example, by the Angular Overlap Model (AOM) (see Chapter 4) and by the Crystal Field. In the crystal field approach [49] , the metal–ligand interaction is treated as purely

electrostatic by thinking of all the species as point charged; electrons and nuclei of surrounding atoms are taken into account by adding in the Hamiltonian a potential field of the same symmetry.

The general Hamiltonian including the interaction with the external magnetic field, to describe the electronic structure of a paramagnetic atom in a complex, is given by (see *e.g.* ref.[52])

$$\mathrm{H} = -\frac{\hbar^2}{2m}\sum_k \nabla_k^2 + V_{EL} + V_C + H_{LS} + H_Z + H_{SS} + H_{SI} + H_{LI} + ... \quad (19)$$

where the first is the electronic kinetics term, V_{EL} is the electronic potential of the free ion, V_C is the crystal field potential, H_{LS} describes the spin–orbit interaction, H_Z takes into account the interaction of the magnetic field and the spin moment of the electrons; H_{SS} includes the interaction between two electron magnetic dipoles; H_{SI} entails the electron spin–nuclear spin interaction; H_{LI} entails nuclear spin–orbit interaction. In the Hamiltonian in eq.(19), only the terms which result to be relevant for our analyzed systems have been explicitly mentioned. In general, other terms, which could be relevant in some cases, need to be included, it e.g. the nuclear quadrupole interaction or the nuclear spin–nuclear spin dipole interactions.

Fe–complexes are usually characterized by an intermediate crystal field, this means that

$$H_{LS} < V_C < H_{EL} \quad (20)$$

with V_C greater than the terms that follow it in the Hamiltonian in eq.(19). Moreover, the relative magnitude of the terms in eq.(19) allows to regard V_C, and the following terms, as perturbations on the ion whose ground state is expressed in terms of the quantum numbers L and S. To evaluate the effect of the crystal field, V_C can be expressed in different forms: as an expansion of

spherical harmonics $Y_{lm}(\theta, \phi)$, or in terms of the L operators [52]. Once the splitting of the d–orbitals has been calculated, the electronic configuration of the metal ion can determined.

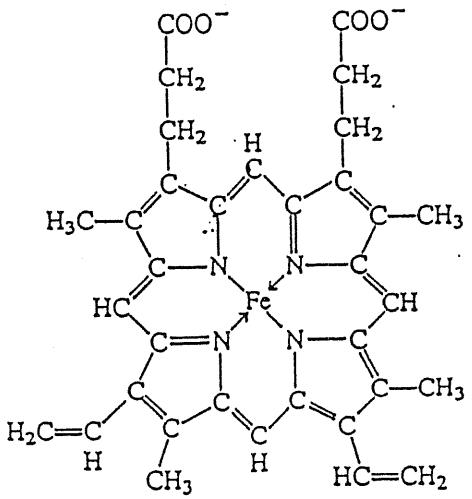

Figure 2.2. Heme structure.

The metal ion in heme proteins is embedded in a ligand field with cubic symmetry. The iron is situated at the center of a porphyrin system and the 1,2,3,4 coordination ligands are given by four nitrogen atoms of the porphyrin ring (see Fig.2.2); the fifth ligand is an imidazole nitrogen of a histidine residue of the protein chain. Finally, in the sixth coordination site, different small ligands can be attached; examples of possible 6th ligands are H_2O ,F^-, CN^-, OH^-, OCN^-, N_3^-, SH^-.

At this point, the perturbation introduced by the other terms in the Hamiltonian can be introduced.

In a purely octahedral field, the d–level of the Fe^{3+} is split into two sublevels (d_{yz}, d_{xz}, d_{xy}) and $(d_{x^2-y^2}, d_{z^2})$. The energy difference between these sublevels is the crystal field splitting and it is indicated by Δ. In general, Δ can assume different values for different 6th ligands. By lowering the symmetry to the

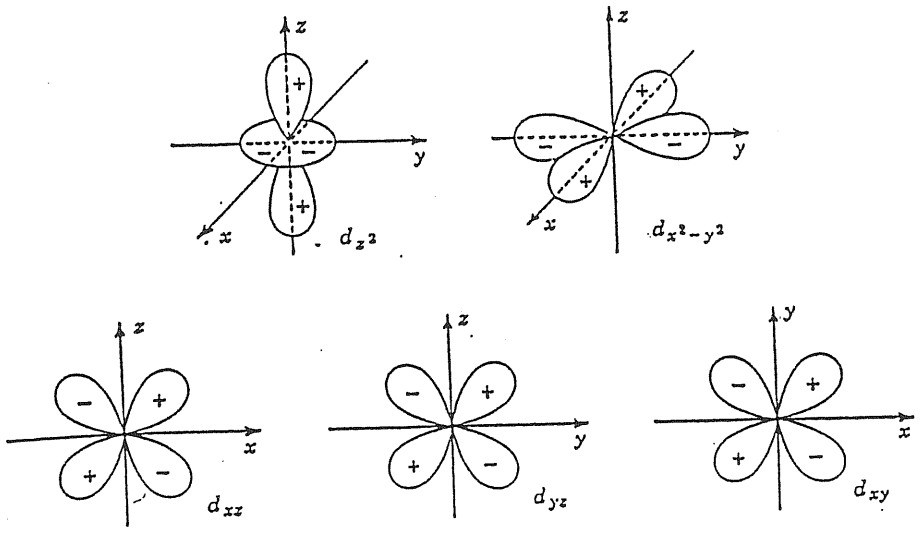

Figure 2.3. Electronic density of d–orbitals.

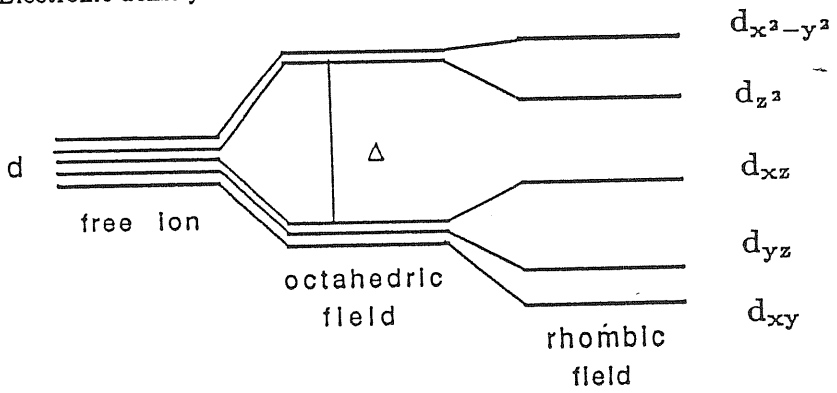

Figure 2.4. Diagram of the splitting of the energy levels in a ligand field of cubic symmetry.

tetragonal, the first sublevel is split into two further sublevels; finally, in rhombic or lower symmetry, all five orbitals have different energies (see Fig.2.3).

Energy levels of the d^5 configuration in cubic ligand field, as function of the strength of the crystal field, have been obtained by a theoretical calculation by Tanabe and Sugano [53]. It results that for weak crystal field, the ground state is the sextet $^6A_1$, the high spin configuration; whereas to a strong crystal field corresponds the doublet $^2T_2$, the low spin configuration (see Fig.2.5).

It should be noted that the energy of the quartet state, $^4T_1$, (an intermediate spin state) is not found in the ground position. Iron in the heme is in a rather

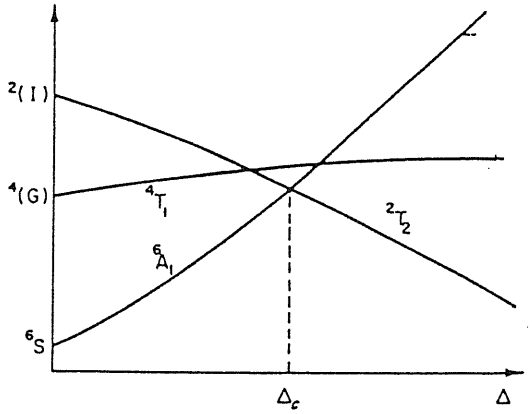

Figure 2.5. Crossing of sextet ($^6A_1$), quartet ($^4T_1$) and doublet ($^2T_2$) levels of ferric ion in cubic ligand field, from ref. [51] .

singular condition in which the high and the low spin states are energetically very near to each other. This property gives to the heme iron a particularly flexible electronic structure. In general, while in the low spin configuration, the iron lies in the heme–plane, in the high spin, it is displaced from the heme group to the proximal histidine side [54].

At this point we analyzed in some detail the high spin state to which our experimental investigation refers. In general, an useful tool to investigate the EPR spectra is represented by the concept of Spin Hamiltonian [49] which involves only spin operators. The idea on which the Spin Hamiltonian is based is to provide an operator, polynomial in the components of an effective spin vector S, to describe the behaviour of the system. The advantage of the Spin Hamiltonian lies in the fact that it offers a simple theoretical framework for quantities, (*e.g.* *g*, *D*) which can be extracted from the EPR spectra.

2.2.1 The high spin state

It is well–known that the EPR spectra at 77 K of aqueous samples of ferric–Mb and ferric–Hb at $pH \sim 7$ are characterized by two resonances, one at $g \simeq 6$

and a weaker one at $g \simeq 2$ (see Fig.2.6). The weak ligand H_3O^+ to the sixth coordination site of iron, determines a high spin state, S=5/2. In a octahedral field, or field of lower symmetry, the system, characterized by the ^6A state, retains its six–fold degeneracy even when spin–orbit coupling is considered to first order, but, in second order, the degeneracy is lifted to give three spaced Kramers doublets.

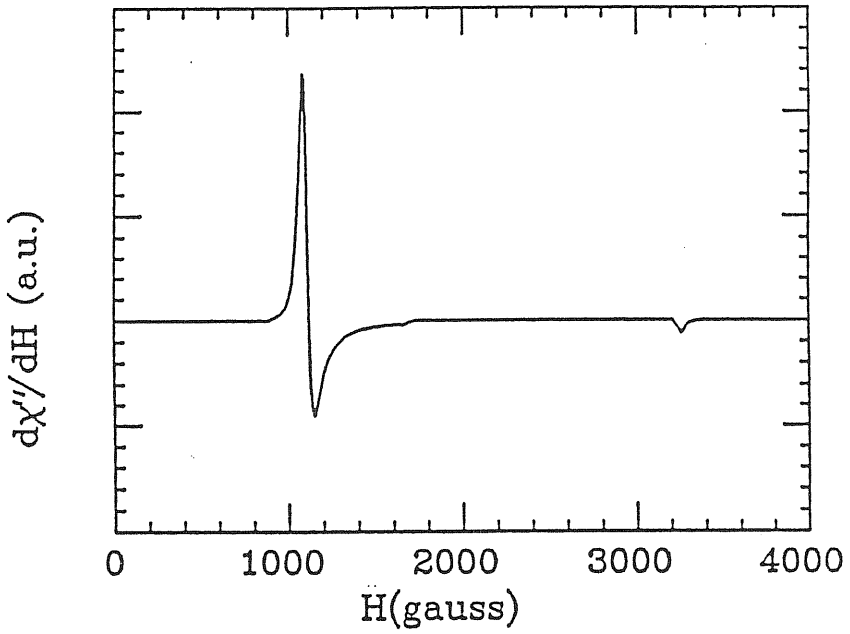

Figure 2.6. It is shown an experimental EPR spectrum, recorded at 77 K, of high spin ferric metMb solution at $pH \simeq 7$.

The system can be described by a second order spin Hamiltonian

$$H_s = g_e \beta \mathbf{H} \cdot \mathbf{S} + D[S_z^2 - S(S+1)/3] + E(S_x^2 - S_y^2) \qquad (21)$$

where g_e is the value for the free electron, given that for an S state is no orbital contribution to the magnetic moment; D and E are the tetragonal and the rhombic zero–field splittings, respectively. For heme proteins, the condition of large zero field splitting is satisfied ($D \sim 10\ cm^{-1}$) [55], only transitions within the lowest Kramers doublet occur, and a fictitious spin S=1/2 can be used to

fully represent the spin Hamiltonian of the system, which for axial symmetry ($g_x = g_y = g_\perp$ and $g_z = g_{||}$) can be expressed by

$$H_s = g_{||}\beta H_z S_z + g_\perp \beta (H_x S_x + H_y S_y) \tag{22}$$

where $g_{||} \simeq 2$ and $g_\perp \simeq 6$ are the g–values which are observed in the experimental spectra. Splitting of the in–plane value into two values, g_x and g_y, may result in a broadening (as in our case) or even in a splitting [56] of the $g \simeq 6$ line. High order corrections, arising from spin orbit mixing of the excited quartet states into the lowest Kramers doublet lead, under the assumption of a four–state model [51,57] [58,59],

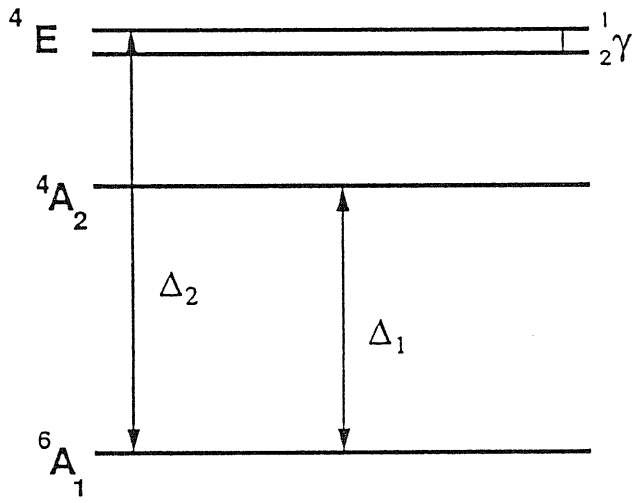

Figure 2.7. Energy level diagram of the low–lying electronic states of high spin ferric heme.

to the following expression for g_x and g_y

$$g_{x,y} = 6.01 \pm 24\frac{E}{D} - 18.7\left(\frac{E}{D}\right)^2 - 12\eta^2 \tag{23}$$

where the tetragonal zero–field splitting D is given by

$$D = \frac{\lambda^2}{5}\left(\frac{1}{\Delta_1} - \frac{1}{\Delta_2}\right) \tag{24}$$

and the rhombic zero–field splitting E is expressed by

$$E = \frac{1}{10}\frac{\gamma\lambda^2}{\Delta_2^2} \tag{25}$$

finally, the spin–orbit mixing of excited quartet states into the lowest Kramers doublet is

$$\eta^2 = \frac{\lambda^2}{5}\left(\frac{1}{\Delta_1^2} + \frac{1}{\Delta_1\Delta_2} + \frac{1}{\Delta_2^2}\right) \tag{26}$$

λ is the effective spin–orbit coupling constant ($\lambda \sim 300\ cm^{-1}$) which is reduced from the free-ion value ($\lambda \sim 420\ cm^{-1}$) ; Δ_1, Δ_2, and γ are the energy difference of the low–lying electronic states of high spin ferric heme (see Fig.2.7).

2.3 Simulation of the EPR spectra

The experimental spectra can be simulated by an appropriate expression for the derivative of the microwave absorption, $dS(\nu, H)/dH$. The net absorption of microwave radiation, between the two levels A and B, $S(\nu, H)$, which is proportional to the imaginary component of the resonant magnetic susceptibility $\chi''(\nu)$, is given by [49]

$$S(\nu, H) = C'\nu\xi\left\{Q_o\frac{N}{Z}e^{-\frac{h\nu}{kT}} \mid < B \mid H_1(t) \mid A > \mid^2 f([\nu - \nu_o], \sigma_\nu)\right\} \tag{27}$$

where C' is a constant which depends on the detection system and the microwave circuit; Z is the partition function; Q_o is the unloaded Q–factor for the cavity, N is the number of spins per unit volume; ν is the microwave frequency and ν_o is the resonance frequency; $f([\nu - \nu_o], \sigma_\nu)$ is the lineshape function centered at the resonance frequency ν_o with a linewidth parameter σ_ν.

For a powder, in which the molecular axes of the heme groups are randomly oriented, such an absorption can be expressed by

$$S(\nu, H) = C\nu\int_0^{\frac{\pi}{2}}\int_0^{\frac{\pi}{2}} P(\theta, \phi) f([\nu - \nu_o], \sigma_\nu)\sin(\theta)d\theta d\phi \tag{28}$$

where C is a constant that encompasses all instrumental parameters, $P(\theta,\phi)$ is the orientation dependent transition probability; finally, the integration over θ and ϕ takes into account for the random orientation of the molecular axes with respect to the magnetic field.

Since usual EPR experiments are performed by sweeping the magnetic field and by keeping the frequency fixed (ν_c) some caution should be exercised when eq.(28) is employed to work out an expression suitable to simulate a field–swept EPR spectrum [60,61]. For systems with S=1/2, if $P(\theta,\phi)$ and σ_ν do not depend upon the magnetic field, the following expression can be used [60]

$$\frac{dS(\nu_c,H)}{dH} = C\frac{\nu_c h}{\beta}\int_0^{\frac{\pi}{2}}\int_0^{\frac{\pi}{2}} \frac{P(\theta,\phi)}{g(\theta,\phi)}\frac{df([H-H_o],\sigma_H)}{dH}\sin(\theta)d\theta d\phi \qquad (29)$$

where $g(\theta,\phi)$ that should be included to take into account for the Aasa–Vanngard [62] correction, is given by

$$g(\theta,\phi) = (g_x^2\sin^2\theta\cos^2\phi + g_y^2\sin^2\theta\sin^2\phi + g_z^2\cos^2\theta)^{\frac{1}{2}} \qquad (30)$$

and $f([H-H_o],\sigma_H)$, the lineshape function centered at the resonance field H_o and with a linewidth parameter σ_H measured in field units, has been introduced to take into account for all the broadening mechanisms not explicitly considered (residual linewidth [61]).

For an S =1/2 system, the orientation–dependent probability $P(\theta,\phi)$, can exactly be expressed by [63]

$$P(\theta,\phi) = g_x^2+g_y^2+g_z^2-\frac{1}{g^2(\theta,\phi)}[g_x^4\sin^2\theta\cos^2\phi+g_y^4\sin^2\theta\sin^2\phi+g_z^4\cos^2\theta] \qquad (31)$$

In the shown simulations, a lorentzian lineshape

$$f([H-H_o],\sigma_H) = \frac{1}{\pi\sigma_H}\frac{1}{\left[1+(\frac{H-H_o}{\sigma_H})^2\right]} \qquad (32)$$

has been employed allowing us to reproduce some details of the experimental spectra that other lineshape functions, (*i.e.* gaussian), were not able to reproduce. Different linewidth parameter values have been used to simulate different EPR spectra.

2.3.1 Isomoto algorithm

The core of simulation method is based on the Isomoto algorithm [63], complemented with the Aasa–Vanngard [62] correction. The range of the magnetic field is divided into N intervals; once the principal values of the g–tensor (g_x, g_y, g_z) have been fixed, the resonance field H_o can be calculated at each orientation (θ, ϕ) by

$$H_o = \frac{h\nu_c}{\beta g(\theta, \phi)} \tag{33}$$

The intensity around the resonance H_o is calculated for M intervals of the field division by

$$\frac{dS(\nu_c, H)}{dH} = \frac{C\nu_c h}{\beta} \frac{P(\theta, \phi)}{g(\theta, \phi)} \frac{df([H_j - H_i], \sigma_H)}{dH} \tag{34}$$

for $i - \frac{M}{2} < j < i + \frac{M}{2}$, where H_i is the field division in which the resonance falls. The field–swept derivative spectrum is computer–generated, by carrying on the integration in eq.(29) as a sum over θ and ϕ

$$\frac{dS(\nu_c, H)}{dH} = \frac{C\nu_c h}{\beta} \sum_{\theta,\phi} \frac{P(\theta, \phi)}{g(\theta, \phi)} \frac{df([H - H_o], \sigma_H)}{dH} \tag{35}$$

The increments for θ and ϕ have been chosen to allow us to limit computer–noise at the required level (computer–noise not greater than the experimental errors). The N and M values that have to be used depend on different factors, for example the analytical expression of the lineshape and the numerical value of the linewidth.

2.3.2 The g–strain effect

The use of eq.(35) is not sufficient to reproduce in a reliable way the EPR spectra of metallo–protein frozen solutions. These spectra are characterized by a large inhomogeneous broadening (g–strain) which is superimposed on all the other broadening effects [32,35] [64–69] and these features cannot satisfactorily be reproduced even if higher values for σ_H are used in eq.(35). Presence of g–strain prevents, in many cases, to reproduce all the characteristics of the EPR spectra by means a single g–tensor in connection with different values of the linewidth parameter σ_H. The variability around the metal ion of the electric field modulating the g tensor is responsible for the g–strain effect. To take into account for this effect, two different approaches are followed in the literature: i) a statistical model [65–67] in which random variations of the electric field are introduced through distributions of the g–tensor components; ii) a physical model [58] [68,69] in which some physical parameters are distributed as consequence of the random variability around the metal ion. In the following simulations, it has been followed a physical approach, and some crystal field parameters have been assumed to be distributed.

If Γ is a generic distributed parameter (or a set of parameters) affecting the g–values, the resulting simulated spectrum can be visualized as a superposition, weighed in a proper way, of different spectra each related to different values of (g_x, g_y, g_z).

In the case in which Γ is given by a gaussian distribution, the simulated EPR derivative spectrum can be finally expressed by

$$\frac{dS(\nu_c,H)}{dH} = \frac{C\nu_c h}{\beta}\frac{1}{2\pi\sigma_\Gamma}\int \frac{dS(\nu_c,H,\Gamma)}{dH} e^{-[\frac{\Gamma-\Gamma^o}{\sigma_\Gamma}]^2} d\Gamma \qquad (36)$$

where, assigned Γ, the corresponding derivative spectrum $dS(\nu_c, H, \Gamma)/dH$ is determined by means of eq.(35).

2.3.3 Fit of spectra

Computer–synthesized spectra have been used to fit the experimental EPR spectra in order to determine the parameters Γ_o and σ_Γ, characterizing the gaussian distribution for Γ.

The bestfit is obtained by a minimization procedure of the χ^2–function

$$\chi^2 = \sum_{i=1}^{N} \left[\frac{I^{exp}(H_i) - I^{sim}(H_i, p)}{\sigma_i} \right]^2 \qquad (37)$$

where $I^{exp}(H_i)$ is the derivative of the experimental EPR absorption spectrum sampled at 200 discrete points of the magnetic field, $I^{sim}(H_i, p)$ is the simulated spectrum that also depends on the parameter set (Γ_o, σ_Γ), finally σ_i is the standard deviation calculated for the i–th experimental point of the EPR spectrum by repeated runs. The search of the bestfit parameters has been done by allowing each parameter to vary over a wide range consistent with both those estimated from the experimental spectra and those reported in the literature [59]. Since no–analytical expression is available for the function to be minimized, the Monte Carlo method, which performs a random search of the bestfit parameters, is particularly suitable to be applied in the present case [70]. We preferred, however, to use a simulated annealing approach [71] to limit computer–time with respect to a standard Monte Carlo procedure. The core of the simulated annealing method is represented by the annealing schedule which determines how the control parameter T, entering in the Metropolis test as the analog of temperature, is lowered from high to low values. The schedule depends on the context and it requires experimentations [72]. Different initial

values for T have been considered for different ranges of parameters. Generally, this value has been held constant for 15 steps and then it is lowered of 50% and so on. When the variation of χ^2 becomes smaller than an arbitrary fixed value, the current search is stopped and a new search is performed by reinitializing the value of T. Sufficiently low values of χ^2 (according to the χ^2–test) must be reached to stop the research of the bestfit parameters.

Chapter 3

EPR spectra of high spin ferric myoglobin

3.1 Materials and experimental methods

Mb EPR samples, at three different pH values, were prepared by dissolving commercial (Sigma Chem. Co.) lyophilized horse skeletal muscle Mb in 0.2 M phosphate buffer. The highest concentration of Mb in the solutions was about 5 mM. Final pHs for the Mb solutions were $pH \simeq 5.6$, $pH \simeq 6.8$ and $pH \simeq 9$. Hb EPR samples were prepared from whole human blood. Erythrocytes were washed three times with 0.9% NaCl and spun at 1200 rpm. Lysis was performed by adding 1.5 volume of distilled water to 1 volume of packed cells, then the ghosts were centrifuged out at 16000 rpm [73]. Final pH of Hb solutions was about 6.8.

Ferricyanide was used to oxidize the heme iron to the ferric valence state and the solutions were dialysed several times against buffers to remove the oxidant. Mb samples in presence of different added solvents were prepared from aqueous Mb solution at $pH \simeq 6.8$. Aliquots of methanol (*Meth*) and ethanol (*Eth*) buffer solutions have been added to Mb aqueous solutions until the required concentration was reached. The final concentration in methanol and ethanol

was about 1:1 to molar heme concentration. Samples in presence of glycerol (*Gly*) have been prepared in 1:1 water–glycerol mixture. Samples in presence of ethylene glycol (*EthGly*) have been prepared in 1:1 water–ethylene glycol mixture. Samples in presence of sucrose (*Sucro*) have been prepared in 1:1 water–sucrose (1 M solution) mixture. All chemicals used were of analytical reagent grade.

A fast cooling rate (*Fast*) has been obtained by dipping the samples into liquid nitrogen at 77 K; while in a slow cooling rate (*Slow*), the system was cooled with a rate of 0.5 deg/min from 300 K to 140 K.

All the EPR spectra were recorded at 77 K by an X–band Varian E109 spectrometer equipped with a variable temperature control which was also used to cool the samples in a controlled way. To calculate the experimental g–values, a magnetic field calibration was performed with a Magnion Precision NMR gaussmeter Mod.G–542; the microwave frequency being measured with a Marconi 2440 counter.

The acquisition of EPR data was carried out on a HP 86A personal computer through a home made interface connected to a IEEE 488 bus [74]. To run both simulations and bestfit programs, the same microcomputer was switched to an intelligent terminal of the main frame computer (VAX 8350), through a serial interface and an HP terminal emulator. Programs were written in Fortran language.

3.2 Analysis of the EPR spectra

EPR spectra, recorded at 77 K, of high spin ferric Mb and Hb samples in

presence of different solvents, at different pHs values and submitted to different cooling rates have been analyzed. Low temperature EPR spectra of high spin Mb and Hb at $pH \sim 7$ are characterized by two resonances, one at $g \simeq 6$ and a weaker one at $g \simeq 2$ (see Fig. 2.6). At $pH \simeq 5.6$ and $pH \simeq 9$, an additional EPR signal corresponding to a low spin configuration is present; however, also in this case, the attention has been put to the $g \simeq 6$ line of the high spin configuration. The $g \simeq 6$ line, which corresponds to the g_x and g_y resonances and in which a lot of information is stored, has been submitted to a careful inspection.

A preliminary analysis of this line can be done by means of some empirical parameters: g_{eff}, the effective g-value of the resonance; *width*, the peak to peak width of the line; and *ratio*, the ratio between the height of the positive and of the negative part of line. These parameters can result very useful into a first characterization of the line.

In Figs.3.1–3.4, the region around the $g \simeq 6$ line of all the analyzed spectra, together to the values of these three parameters, is shown.

First of all, it should be noted that the values of g_{eff}, *width* and *ratio*, of pure Mb and Hb samples, result to be in agreement with the experimental values reported in literature [56]. Moreover, on base of these values, different observations can be done. It can be seen that the $g \simeq 6$ lines of Mb and Hb samples are quite different; in particular, the line corresponding to Hb samples results to be larger with respect to the Mb line.

In general, it can be observed that the composition of solvent in which the protein is embedded, the pH value of the solution, and the cooling rates to which the samples have been submitted, result to affect the EPR spectra. Although the modifications of the $g \simeq 6$ line, as seen through the values of parameters

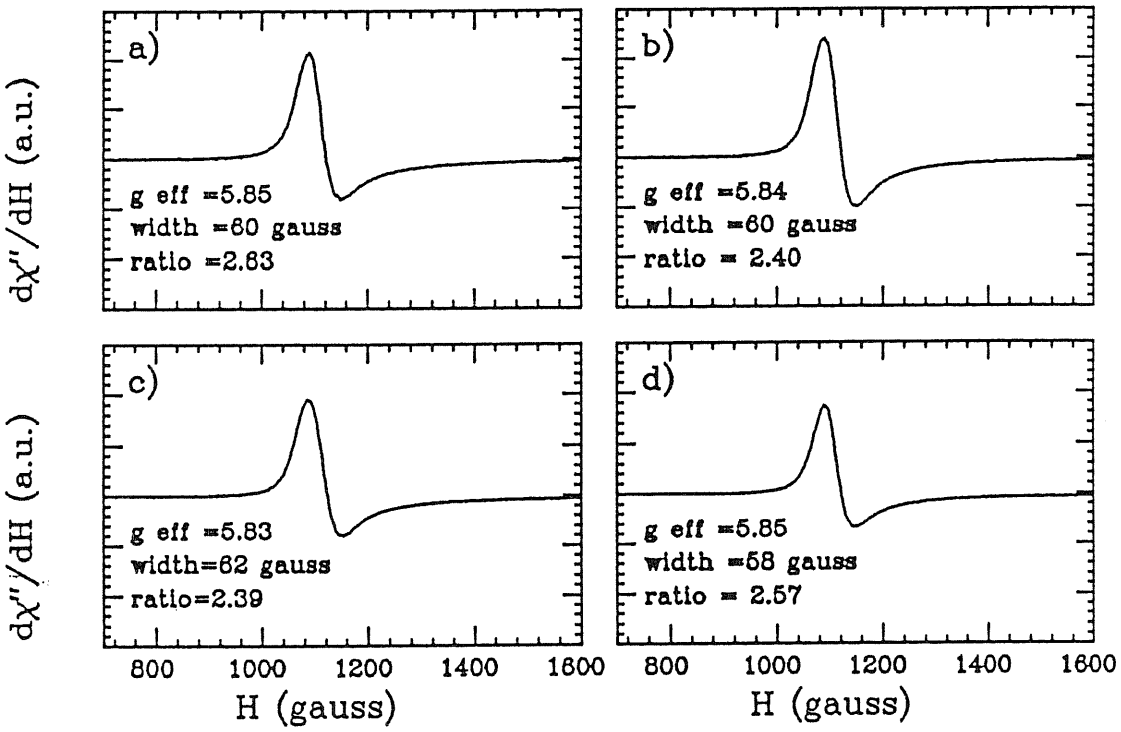

Figure 3.1. The experimental g=6 line of X-band EPR spectra, recorded at 77 K, related to high spin ferric Mb solutions in different conditions, submitted to fast cooling rate, are shown. a) pure Mb solutions; b) Mb solutions with added glycerol (1:1 by volume); c) Mb solutions with added ethylene glycol (1:1 by volume); d) Mb solutions with added sucrose (1 M). In all the cases the values of the parameters g_{eff}, *width* and *ratio* are reported.

ratio, *width* and g_{eff}, are quite small, they are significant.

The most sensitive parameter seems to be the *ratio* which shows a close dependence on the conditions in which the EPR spectra have been recorded. A closer inspection is required in order to understand the meaning of these observed differences in the EPR spectra. A quantitative analysis of EPR spectra can be done by means of simulation whose general principles have been presented in Chapter 2. First of all, it should be noted that some attempts to simulate high spin ferric Mb and Hb EPR spectra with a single g-tensor, in connection with different lineshape expressions and with different values of the linewidth parameter σ_H, have been done. These attempts did not allow us to reproduce all the details of the spectra. As we have already mentioned, in many cases,

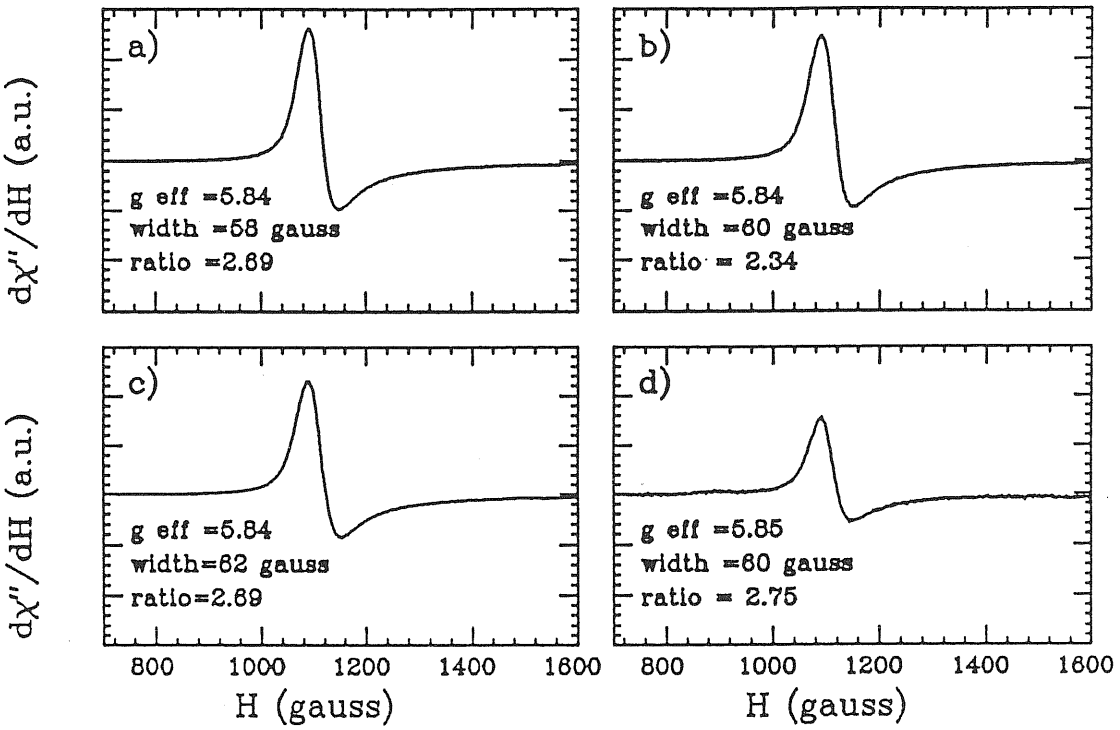

Figure 3.2. The experimental g=6 line of X-band EPR spectra, recorded at 77 K, related to high spin ferric Mb solutions in different conditions, submitted to fast cooling rate, are shown. a) Mb solutions with added methanol (1:1 molar heme concentration); b) Mb solutions with added ethanol (1:1 molar heme concentration); c) pure Mb solutions at pH equal to 5.6; d) pure Mb solutions at pH equal to 9. In all the cases the values of the parameters g_{eff}, $width$ and $ratio$ are reported.

EPR spectra of metallo–proteins solutions are characterized by the presence of a large inhomogeneous broadening to which corresponds a spread in the g–tensor values (g–strain). For example, Mb and Hb EPR spectra, at different pH and in presence of a small amount of methanol and ethanol, have been interpreted by assuming that the ratio between the rhombic and the tetragonal zero–field splitting parameters and the spin–orbit mixing parameter are distributed [12,58]. There are different types of indications pointing out that, in Mb, this spread is to be attributed to a spread of energy differences of the low–lying electronic states [59,75]. In this context, we have tried to simulate our spectra by assuming that the crystal field parameters Δ_1 and Δ_2 are distributed around a mean

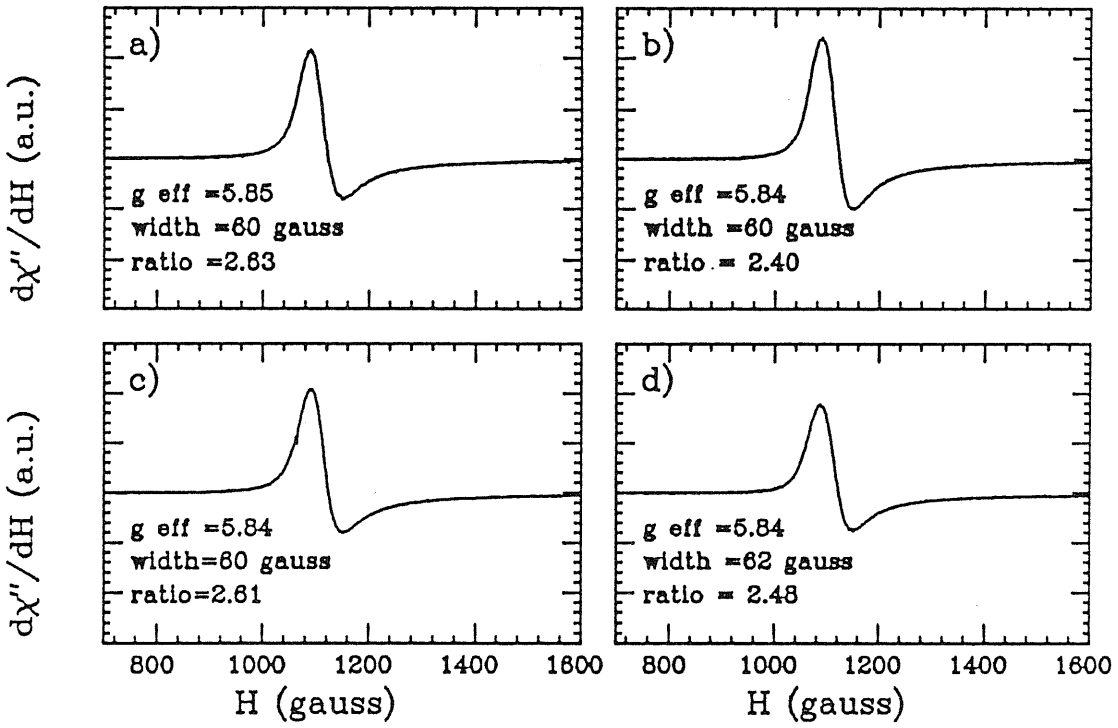

Figure 3.3. The experimental g=6 line of X–band EPR spectra, recorded at 77 K, related to high spin ferric Mb solutions in different conditions, submitted to fast and slow cooling rate, are shown. a) pure Mb solutions submitted to fast cooling rate; b) Mb solutions with added glycerol (1:1 by volume) submitted to fast cooling rate; c) pure Mb solutions submitted to slow cooling rate; d) Mb solutions with added glycerol (1:1 by volume) submitted to slow cooling rate. In all the cases the values of the parameters g_{eff}, $width$ and $ratio$ are reported.

value. This fact can be visualized by a shaded region around the level of the $^6A_1$, $^4A_2$ and ^4E states (see Fig.3.5). In order to simulate our spectra, two independent gaussian distributions for Δ_1 and Δ_2 have been introduced. In principle, there is not any reason for which Δ_1 and Δ_2 should be independent; some attempts to correlate these parameters have been done. Anyway, better results have been reached with Δ_1 and Δ_2 assumed independent. It has been, moreover, assumed that a small rhombic distortion is present in the system. A rhombic distortion causes the d_{xz} and d_{yz} orbitals of the iron, that in tetragonal symmetry are degenerate, to be split (see Fig.2.4). This perturbation then results into a splitting of the ^4E state into $^4E_1$ and $^4E_2$ whose difference is

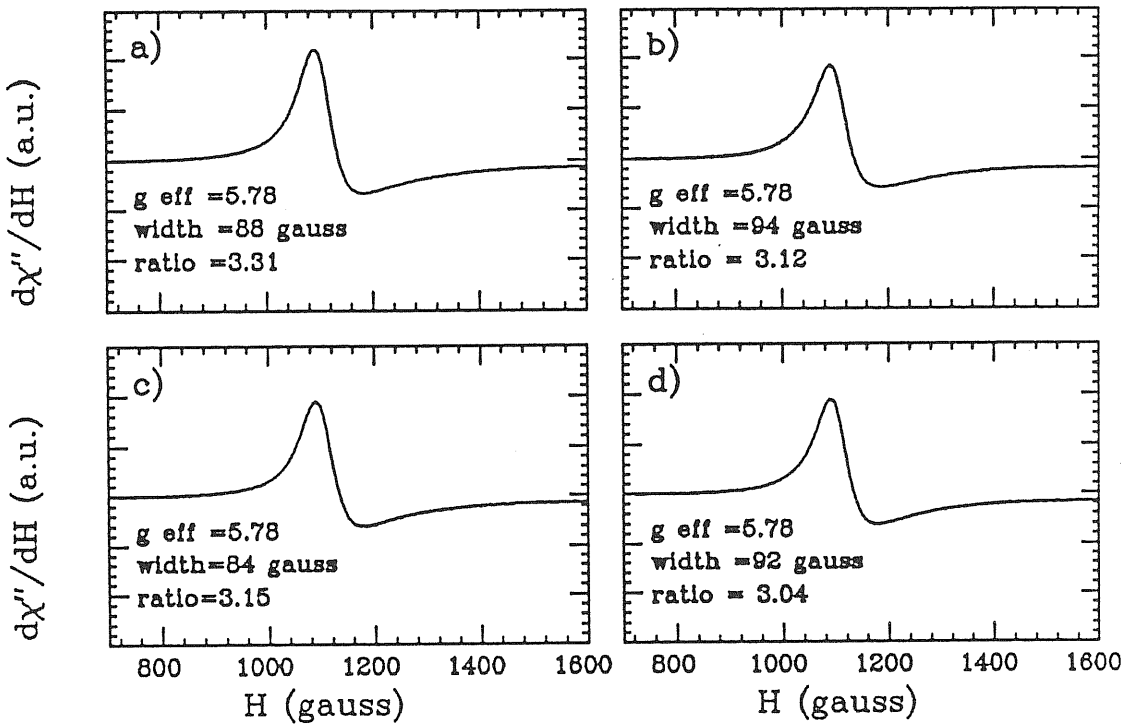

Figure 3.4. The experimental g=6 line of X-band EPR spectra, recorded at 77 K, related to high spin ferric Hb solutions in different conditions, submitted to fast and slow cooling rate, are shown. a) pure Hb solutions submitted to fast cooling rate; b) pure Hb solutions submitted to slow cooling rate; c) Hb solutions with added glycerol (1:1 by volume) submitted to fast cooling rate; d) Hb solutions with added glycerol (1:1 by volume) submitted to slow cooling rate. In all the cases the values of the parameters g_{eff}, $width$ and $ratio$ are reported.

put equal to γ (see Fig.3.5). A value of about $\gamma \simeq 60\ cm^{-1}$ has been assumed in agreement with the value presented by Fiamingo *et al.*[59]. In general, it is possible that also γ might be distributed, however, since this contribute is smaller than the other ones, this additional effect has not been considered.

Concerning the lineshape, some details should be given. A residual lineshape, including all the broadening mechanisms that are not explicitly considered in the simulation, has been introduced in eq.(36). For EPR spectra of high spin heme–proteins, the most significant broadening mechanisms are the unsolved hyperfine splitting and a smaller contribute due to the relaxation time T_1. For the heme–proteins samples recorded at 77 K, these contributes can be satisfacto-

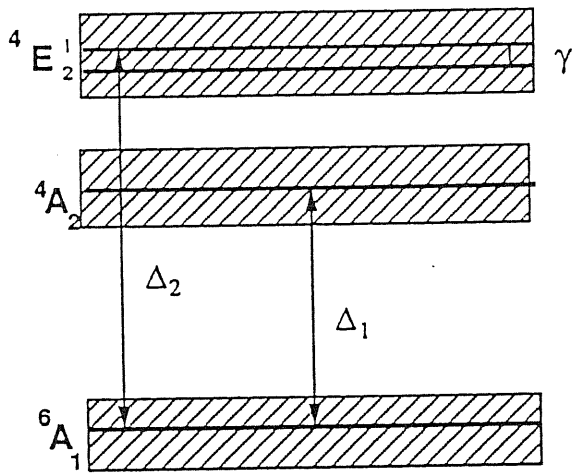

Figure 3.5. Energy level diagram of the low lying electron states of high spin ferric heme. The shaded regions indicate the variability of the energy levels (not in scale).

rily expressed by a Lorentzian lineshape with a linewidth parameter $\sigma_H = 25$ gauss, for Mb, and $\sigma_H = 33$ gauss, for Hb samples.

3.3 Results

In Fig.3.6, together with the experimental spectra also the corresponding simulated spectra (dashed lines), for pure Mb and pure Hb samples, are shown. These simulated spectra have been obtained by means of eq.(36) in which the Γ distribution has been substituted with the Δ_1 and Δ_2 distributions.

The agreement between experimental and simulated patterns appears very good; however the goodness of the fit has been confirmed, in each case, by the χ^2–test (see Chapter 2).

In Table 1, the parameters Δ_1^o, σ_{Δ_1}, Δ_2^o, and σ_{Δ_2}, as obtained by simulations of the EPR spectra from Mb samples in different conditions and submitted to different cooling rates are reported; in Table 2, the values of the same parameters from simulations of EPR spectra related to Hb samples in absence and in presence of glycerol and submitted to fast and slow cooling rate, are shown.

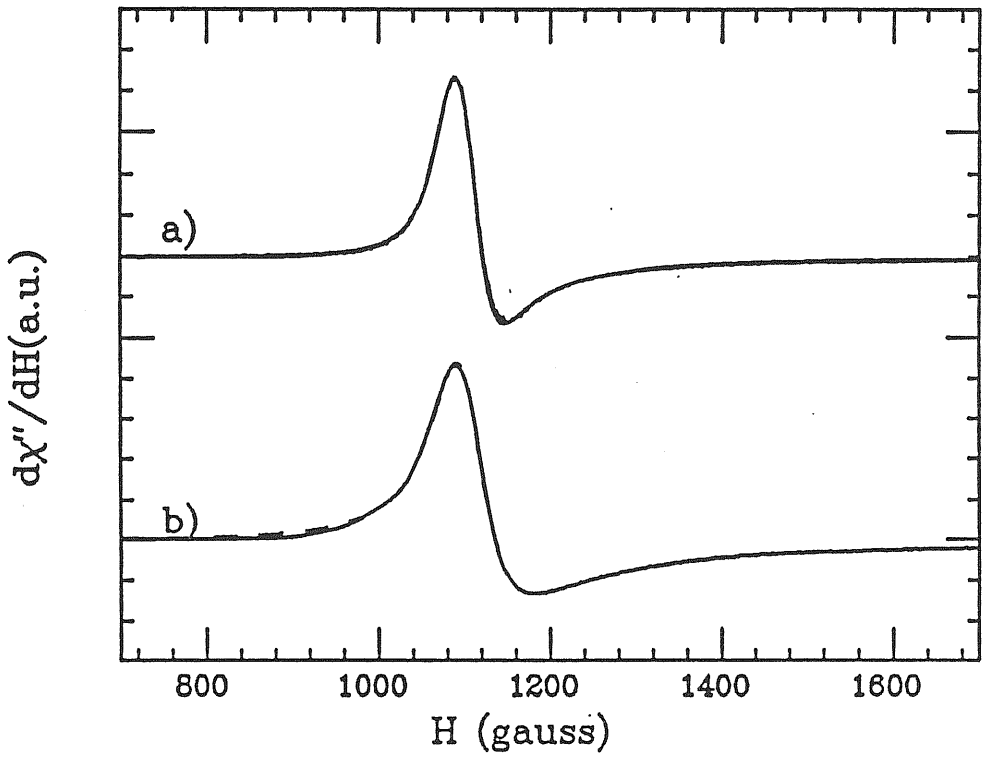

Figure 3.6. The superposition of the experimental (continuous line) and simulated (dashed line) g=6 line of X-band EPR spectra related to fast cooled high spin ferric pure Mb (a) and Hb (b) solutions are shown.

The physical soundness of the simulations performed can be assessed by considering the central values of the Δ_1 and Δ_2 distributions. Concerning Mb, the values obtained for fast cooled aqueous solutions are very close to those measured by EPR in crystals and aqueous frozen solutions of Mb [59]. Similar data are not available for Hb samples, however, if the D,E and η values, experimentally determined and existing in the literature [56,58], are fed into eqs.(24–26), values for Δ_1 and Δ_2 quite close to ours are obtained.

TABLE 1 The central values and the root of variances of the gaussian distributions related to the crystal field parameters Δ_1 and Δ_2 are reported. These values have been obtained by simulations of the $g \simeq 6$ line of the EPR spectra, recorded at 77 K, of Mb aqueous solutions in different conditions. If it is not explicitly mentioned, the pH of solutions is about 7. The 68% confidence limits are given, in percentage, by 3% for Δ_1°, 25% for σ_{Δ_1}, 3% for Δ_2° and 25% for σ_{Δ_2}. For abbreviations see section 3.1.

SAMPLE	$\Delta_1^\circ\ cm^{-1}$	$\sigma_{\Delta_1}\ cm^{-1}$	$\Delta_2^\circ\ cm^{-1}$	$\sigma_{\Delta_2}\ cm^{-1}$
Mb (Fast)	2266.	259.	5759.	936.
Mb+Gly (Fast)	2194.	280.	5500.	549.
Mb+EthGly (Fast)	2248.	248.	5422.	619.
Mb+Sucro (Fast)	2181.	231.	5646.	625.
Mb+Meth (Fast)	2148.	231.	5658.	835.
Mb+Eth (Fast)	2156.	263.	5465.	803.
Mb pH=5.6 (Fast)	2232.	215.	5400.	910.
Mb pH=9 (Fast)	2160.	228.	5642.	877.
Mb (Slow)	2250.	238.	5750.	920.
Mb+Gly (Slow)	2248.	232.	5417.	516.

3.3.1 Cooling rate effects

In general, it can be observed that a slow cooling rate yields quite small modifications in the Δ_1 and Δ_2 distributions. In particular, when the samples are submitted to a slow cooling rate, the central values of the distributions, Δ_1° and Δ_2°, change with respect to fast cooled samples less than 2% in Mb and in Hb samples in presence and in absence of glycerol.

More significant are the changes in the widths σ_{Δ_1} and σ_{Δ_2} of the distributions. In Mb, slow cooling rate causes a lowering of these parameters: σ_{Δ_1} decreases of 8% in samples without glycerol, and of 14% in samples with glycerol; σ_{Δ_2} is

TABLE 2 The central values and the root of variances of the gaussian distributions related to the crystal field parameters Δ_1 and Δ_2 are reported. These values have been obtained by simulations of the $g \simeq 6$ line of the EPR spectra, recorded at 77 K, of Hb aqueous solutions in different conditions. The pH of solutions is about 7. The 68% confidence limits are given, in percentage, by 3% for Δ_1^o, 25% for σ_{Δ_1}, 3% for Δ_2^o and 25% for σ_{Δ_2}. For abbreviations see section 3.1.

SAMPLE	$\Delta_1^o\ cm^{-1}$	$\sigma_{\Delta_1}\ cm^{-1}$	$\Delta_2^o\ cm^{-1}$	$\sigma_{\Delta_2}\ cm^{-1}$
Hb (Fast)	2155.	619.	420.	1663.
Hb+Gly (Fast)	2169.	621.	4561.	1549.
Hb (Slow)	2153.	576.	4685.	1629.
Hb+Gly (Slow)	2107.	515.	4547.	1487.

decreased of 2% and 6%, respectively in absence and in presence of glycerol. For Hb, in samples without glycerol, σ_{Δ_1} and σ_{Δ_2} decrease of 7% and 2%, respectively, as consequence of slow cooling rate; while in samples in presence of glycerol, these parameters are lowered of 17% and of 4%.

3.3.2 Effects induced by changes in the solvent composition

In general, the Δ_1 and Δ_2 distributions are modified by the presence of the added solvents in a large quantity to the solutions; however, the Δ_2 distribution, and in particular the σ_{Δ_2} parameter, is stronger affected by the solvent composition of protein solution. In this context, it should be noted that small addition of glycerol, ethylene glycol and sucrose (*e.g.* 1:1 heme molar concentration) leads to no change in the EPR spectrum, and then also in the crystal field parameter distributions.

In order to stress these effects, the results shown in Table 1 can be expressed in

terms of variations of the crystal field parameters with respect to those related to pure fast cooled Mb solutions.

Concerning the Δ_1 distribution, it can be observed a reduction, of the Δ_1^o parameter of about 3.2%, 0.8% and 3.8% for samples in presence of glycerol, ethylene glycol and sucrose, respectively. The σ_{Δ_1} parameter increases of 8% in presence of glycerol, while it decreases of 4.2% in presence of ethylene glycol and of 11% in presence of sucrose.

Regarding the Δ_2 distribution, Δ_2^o and σ_{Δ_2} always decrease with respect to pure Mb solution, as consequence of solvent addition; in particular, Δ_2^o decreases of 4.5%, 5.8% and 2% while σ_{Δ_2} decreases of 41%, 34% and 33% for samples in presence of glycerol, ethylene glycol and sucrose, respectively.

A similar behaviour can be observed for what concerns Hb samples. The addition of glycerol yields small changes in Δ_1^o and Δ_2^o, in particular of 0.6% and 1.2%; while σ_{Δ_1} and σ_{Δ_2} decrease of 0.4% and 6.8%, respectively. It should be noted that these changes result smaller with respect to those observed in Mb samples.

3.3.3 Effects induced by addition of small amount of alcohols

Addition of small amount of methanol and ethanol, which, on the other hand, in large quantity cause denaturation of protein, yields significant, but not very large variations in all the crystal field parameters characterizing the Δ_1 and Δ_2 distributions in Mb solutions. In particular, Δ_1^o diminishes of 5.2% and of 4.8%, while Δ_2^o decreases of 1.7% and 5.8% in samples with methanol and ethanol, respectively.

Concerning variances, it can be observed that the presence of methanol yields

a reduction in σ_{Δ_1} of about 11%, and in σ_{Δ_2} of 1.5%; while in solution with ethanol, σ_{Δ_1} increases of 1.5% and σ_{Δ_2} decreases of of 1.5%.

3.3.4 Effects induced by pH changes

Deviations of pH from the physiological values ($pH \simeq 7$) cause modifications in both the Δ_1 and Δ_2 distributions. Both an increase of pH ($pH \simeq 9$) and a lowering of pH ($pH \simeq 5.6$) yield the parameters characterizing the Δ_1 and Δ_2 distributions to be lower. In particular, Δ_1^o decreases of 1.5% and of 4.7%, in solutions with pH=5.6 and pH=9, respectively; while Δ_2^o decreases of 6.2% and of 2%, respectively. The most significant changes are in the parameter σ_{Δ_1}, which is decreased of 17% in solutions at pH=5.6, and it is decreased of 12% in solutions at pH=9. Concerning σ_{Δ_2}, changes are lower, anyway significant; a reduction of 2.8% for Mb solutions at pH=5.6 and a reduction of 6.3% for solutions at pH=9 are observed.

3.4 Discussion

The use of the simulation method outlined in Chapter 2 has allowed us to extract the parameters, characterizing the distribution of the ligand field energies Δ_1 and Δ_2, from the experimental EPR spectra of Mb and Hb samples in different conditions.

The fact that the central values (Δ_1^o and Δ_2^o) of these distributions are found to be consistent with the experimental data reported in the literature and the goodness of the fits are indicative of the reliability of the computer model used. The changes of the central values of the distributions could be interpreted in

terms of modifications of the average structural properties of the protein ensemble. This means that angles between iron and ligands might be modulated by the different conditions to which the protein is submitted.

The results reported in Tables 1 and 2 show also that a significant spread (characterized by the parameters σ_{Δ_1} and σ_{Δ_2} of the distributions) of the crystal field parameters occurs in the ferric heme–proteins investigated.

The widths of the Δ_1 and Δ_2 distributions are to be discussed in close connection to the presence of the protein CS distribution [11,35] [58,76]. Actually, frozen metallo–protein solutions, which are similar to glassy systems with respect to the microscopic disorder displayed by their structure, are characterized by the presence of a static ensemble of frozen CS. To such a conformational heterogeneity corresponds an heterogeneity in the orientation and/or position of the ligand groups that the protein molecule provides to the metal ion. Consequently, the Fe^{3+} ion ligand bonds are modulated (as regards the angles and the distances) according to the microenvironmental fluctuations. The statistical distribution of the atom coordinates will then result in a distribution of the ligand field parameters. In the framework of the crystal field theory, such a physical situation can be taken into account by considering a random distribution of the Δ_1 and Δ_2 energy differences which, through a modulation of the g components, affects the EPR linewidth as observed.

It should be, moreover, noted that an additional source of structural heterogeneity could be represented by the strain imposed, on the protein structure, by the phase transition occurring in the solvent at the freezing point. These freezing–induced effects, which might be superimposed on other effects, are correlated to the ice–crystal dimensions and they can be minimized in the presence of some added solvents (glycerol, ethylene glycol) [69], or by submitting the sam-

ples to slow cooling rate [11,35]. This phenomenon can affect, in a different way, various parts of the protein structure; for example, some artifacts in the ligand orientation and some modifications in the spin equilibrium have been observed according to the freezing procedure [77,78].

3.4.1 Cooling rate effects

The results shown in Tables 1 and 2 point out that the cooling rate can affect the spread of the crystal field parameters. In particular, a slow cooling rate yields a lower width, with respect to fast cooled samples, for the Δ_1 and Δ_2 distributions both in Mb and Hb samples. Such an effect is observed both in the presence and in the absence of glycerol. Different explanations could be invoked for this effect. It cannot be ruled out *"a priori"* the possibility that a different ice–crystal growth, as induced by a slow cooling rate, could eliminate or minimize the above mentioned freezing strains. In this context, it should be recalled that a significant variation in the low field EPR spectra of copper plastocyanin has been observed by controlling the ice–crystal growth through the addition of glycerol to the protein solutions [65]. However, it can be observed that, since the cooling rate effects are quite small, the spread in the crystal field parameters are confirmed to be not totally explainable by the artifacts due to the freezing procedure.

Other possible explanations could be invoked in the assumption that the cooling rate could affect the CS distributions. Some interpretations of this fact will be presented in the next Chapter.

3.4.2 Effects induced by solvent composition

Table 1 shows that the presence of glycerol, ethylene glycol, and sucrose yields a narrowing of the crystal field parameters distribution. As we have already mentioned, glycerol and ethylene glycol can act on the ice–crystal growth by decreasing the strain induced by freezing. It is likely that some contribute to the observed broadening of the crystal field parameters may come from the freezing procedure, however, by taking into account that slow cooling rate does not result in large changes and also the evidences in literature [58], the main contribute should be attribute to an intrinsic heterogeneity of the system.

In general, it should be noted that addition of glycerol, ethylene glycol and sucrose can cause modifications in the solvent properties, and then induce changes in the protein structure and also in the CS distribution. Then, the observed changes in the crystal field parameter distributions, could arise from these effects.

To a deeper analysis, by considering the Δ_1 and Δ_2 distributions separately, it seems that the presence of added solvents essentially affects, in both Mb and Hb solutions, the Δ_2 distribution by decreasing σ_{Δ_2}. This fact seems to point out that the crystal field parameter Δ_2 is connected to those aspects of protein dynamics on which the considered solvents can act in a more direct way.

3.4.3 Effects induced by addition of small amount of alcohols

Since the small quantity of these added alcohols, the observed effects on the crystal field parameter distributions cannot be attributed to a modification of the solvent properties. On the other hand, it is known that methanol binds to the metal ion [79], therefore, it can induce, in a direct way, modifications on

surroundings of the iron. This means that changes in the crystal field parameters should be put into relation to some modifications in the arrangement of ligands around the metal ion.

The fact that alcohols, at these concentrations, can really affect the crystal field parameter distributions has been also adduced as a confirmation of the possibility, for the EPR technique, to visualize the CS distribution in metallo–proteins [58]. One would not expect that alcohols, at the low concentrations employed, affect significantly the freezing of the protein solutions. Then, the spread in the Δ_1 and Δ_2 distributions, which, moreover, depends on the particular added alcohol, probably arises from an intrinsic heterogeneity of the protein solution.

3.4.4 Effects induced by pH changes

The quite small modifications in the crystal field parameter distributions seem to point out that the large deviations of pH, from the physiological value, do not result in drastic change in the protein solutions. However, since modifications in both the solvent properties and in the protein structure, as induced by pH changes, are expected, the observed modifications in the crystal field parameter distributions could be attributed to such effects. It should be also noted that changes in pH values could also yield some freezing–induced effects, through modifications of solvent properties (for example modifications of the network of hydrogen bonds).

3.4.5 Differences between Mb and Hb

Concerning the observed differences between Mb and Hb samples, it can be put into evidence that the values characterizing the crystal field parameter

distributions are quite different for Mb and Hb samples, (see Tables 1 and 2). In particular the widths of the distributions σ_{Δ_1}, σ_{Δ_2} result much larger in Hb than in Mb samples. Nevertheless, the modifications in the crystal field parameter distributions, as induced by slow cooling rate and by addition of glycerol, show a simular behaviour in both the proteins. Since the exposition of the metal ion to the solvent is quite different in these two proteins [80], changes in the heterogeneity around the metal ion are probably mediated by the protein milieu globally, rather than being determined by variations in the local coupling of the solvent to the heme pocket.

On the contrary, addition of glycerol yields variations on σ_{Δ_2} much larger in Mb than in Hb samples. In this case, a different exposition of the active site with respect to external environment could be crucial. An active site more exposed to the bulk, as in the Mb molecule, experiences, in a more direct way, modifications of the solvent; while, in a less exposed site, changes of the solvent should result mediated by the protein matrix and then result weaker. In this respect, the study of the separated α and β Hb polypeptide chains could provide more conclusive information about the role of the solvent and the interplay between chains in Hb.

3.5 Summary

The spread in the crystal field parameter distributions, extracted by EPR spectra of Mb and Hb samples in different conditions, should be regarded as induced by an intrinsic heterogeneity in the protein structure. Such a heterogeneity can be due to to the presence of CS distribution which also could result in a heterogeneity in the microenvironmental around the metal ion. An additional

effect due to freezing procedure cannot be excluded, but its contribute seems to be smaller with respect to the other ones. The CS distribution is affected by the composition of the solvent, by the pH value, by small amount of added alcohols, and also by the cooling rate to which samples have been submitted. At this point, it is required to analyze the crystal field distributions Δ_1 and Δ_2 in terms of a structural heterogeneity in the microenvironment around the metal ion. In other words, the changes in the microenvironment of the heme–group, which result into modifications of the Δ_1 and Δ_2 parameters, should be put into relation to the presence of the CS distribution. A model which connects the spread of the crystal field parameters to CS distribution will be presented in the next Chapter.

Chapter 4

Application of AOM to high spin ferric myoglobin

4.1 General principles of AOM

The Angular Overlap Method (AOM) was originally developed by Schäffer and Jorgensen [81] to rationalize the energies of orbitals in metal complexes. This method, which is a simplification of the LCAO-MO method, can be employed to evaluate the splitting of the Fe^{3+} d–orbitals, as induced by the presence of the ligands.

The AOM takes its name and gains its power by representing the overlap integral S between two orbitals as a simple product of radial and angular terms

$$S = S_\lambda(r) F_{\lambda,\omega} \tag{38}$$

$S_\lambda(r)$ depends upon the distance between the two atomic centers, the nature of atoms and the types of orbitals; $S_\lambda(r)$ is also dependent upon whether the overlap has local $\lambda = \sigma, \pi$ or δ symmetry. The angular term $F_{\lambda,\omega}$ is a simple function of the angular polar coordinates θ, ϕ of one atom relative to another; different functions being found for different values of λ.

In the AOM basic approach, it can be shown (see *e.g.*ref. [82]) that the energy change, e_λ, of a given metal orbital, as induced by a ligand on the z–axis, is

given by

$$e_\lambda = K_\lambda S_\lambda^2 F_{\lambda\omega}^2 \tag{39}$$

In the Wolfsberg–Helmholts approximation [83], the K_λ constant results to be

$$K_\lambda \simeq \frac{H_L}{H_M - H_L} \tag{40}$$

where H_M and H_L are the metal and ligand orbital energies, respectively.
If the ligand is not on the z-axis, a rotation of the coordinates is required. Under the assumptions that the effects of different ligands, on a given metal orbital, are additive and that the ligand–ligand overlap can be neglected, it can be shown that the general ligand field matrix element can be expressed as

$$< \phi_i \mid V \mid \phi_j >= \sum_{\lambda\omega} \sum_{n}^{N} e_{\lambda n} F_{\lambda\omega}(\phi_i, X_n) F_{\lambda\omega}(\phi_j, X_n) \tag{41}$$

where V is the potential induced by the ligands; the first sum on the metal orbitals is referred to a coordinate system x'y'z' such that the i–ligand is on the z' axis; the second sum is extended to the N ligands X_n. $F_{\lambda\omega}(\phi_i, X_n)$ and $F_{\lambda\omega}(\phi_j, X_n)$ are the columns of the AOM rotation matrix which relates the metal orbitals in the primed and unprimed coordinate system (for the angular dependence of the Overlap Integrals see Tables in ref. [82]).
Given a system of assigned geometry, in order to evaluate the matrix elements in eq.(41), three independent parameters, e_σ, $e_\pi$and e_δ, for each ligand are required. In our case, it seems feasible to neglect δ bond effects, and only two parameters for each ligand are used. In general, the semiempirical parameters e_λ could be theoretically evaluated or deduced from experimental data [84].

4.2 Application of AOM to high spin ferric Mb

The crystal field parameters Δ_1 and Δ_2 can be expressed in terms of two different contributes; the splitting of the d–orbitals, induced by the presence of the ligand field, can be evaluated by means of the application of the AOM; and the electrostatic contribute can be expressed in terms of the Racah parameters. For cubic symmetry, the electronic configurations of the states ${}^6A_1$, ${}^4A_2$, ${}^4E_1$ and ${}^4E_2$ in Fig.2.7, are given by

$$\begin{aligned}
{}^6A_1 &\rightarrow \xi^+\eta^+\varsigma^+\theta^+\epsilon^+ \\
{}^4A_2 &\rightarrow \xi^+\eta^+\varsigma^2\theta^+ \\
{}^4E_1 &\rightarrow \frac{1}{2}\xi^+\eta^2\varsigma^+\theta^+ + \frac{\sqrt{3}}{2}\xi^+\eta^2\varsigma^+\epsilon^+ \\
{}^4E_2 &\rightarrow \frac{1}{2}\xi^2\eta^+\varsigma^+\theta^+ + \frac{\sqrt{3}}{2}\xi^2\eta^+\varsigma^+\epsilon^+
\end{aligned} \tag{42}$$

where the symbols ξ, η, ς, θ and ϵ stand for the one electron levels d_{yz}, d_{xz}, d_{xy}, d_{z^2}, and $d_{x^2-y^2}$, respectively. The electrostatic contribute to each electronic state, expressed in terms of the Racah parameters B and C, is given by

$$\begin{aligned}
{}^6A_1 &\rightarrow 10\ A - 35\ B \\
{}^4A_2 &\rightarrow 10\ A - 13\ B + 7\ C \\
{}^4E_1 &\rightarrow 10\ A - 25\ B + 5\ C \\
{}^4E_2 &\rightarrow 10\ A - 24\ B + 5\ C
\end{aligned} \tag{43}$$

From eqs.(42–43) and from the definition of Δ_1 and Δ_2 (see Fig.2.7), it follows

$$\Delta_1 = E({}^4A_2) - E({}^6A_1) = [E(\varsigma) - E(\epsilon)] + [22B + 7C] \tag{44}$$

and

$$\Delta_2 = E({}^4E) - E({}^6A_1) = \frac{1}{2}\{10B + 5C] + [11B + 5C]\} +$$

$$\frac{1}{2}\left\{\frac{1}{4}\left[E(\eta)-E(\epsilon)\right]+\frac{3}{4}\left[E(\eta)-E(\theta)\right]+\frac{1}{4}\left[E(\xi)-E(\theta)\right]\right\} \qquad (45)$$

It is known that the heme complex in metMb is a six–coordinate compound arranged in tetragonal symmetry to which a small rhombic distortion should be added. For sake of simplicity, we assume that the four ligands of the heme–plane are equivalent; in this case only six parameters, instead of twelve, are required to apply the AOM.

Concerning the geometric arrangement of the ligands around the metal ion in Mb, there are many experimental evidences pointing out that, in the high spin configuration, the iron, in both ferrous and ferric form, is displaced out of the heme–plane to the proximal histidine side. In ferric Mb, this displacement, called a, is about 0.40 $\mathring{A}$ [54] (while in ferrous Mb, it is about 0.45 $\mathring{A}$ [85]).

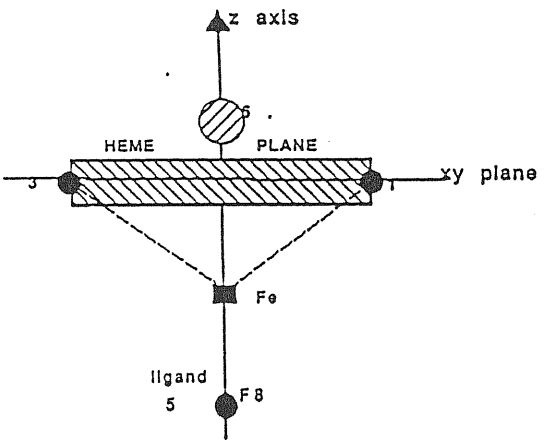

LIGAND	θ	φ
1	90°	0°
2	90°	90°
3	90°	180°
4	90°	270°
5	180°	0°
6	0°	0°

Figure 4.1. It is shown the geometrical arrangement of the ligands around the metal ion in the heme–complex. The values of the angles θ and ϕ employed in the AOM approach, are reported for each ligand.

In Fig.4.1, the arrangement of ligands around the metal ion, together to the values of the angles θ and ϕ characterizing the positions of these ligands, are shown.

The following symbols for the AOM parameters have been employed: e_σ^I and e_π^I to describe the four equivalent ligands of the heme–plane; e_σ^{II} and e_π^{II} to

describe the ligand in fifth position, *i.e.* the N atom of the imidazole belonging to the proximal histidine; finally, e_σ^{III} and e_π^{III} have been associated to the ligand in the sixth position (*i.e.* the bound water molecule).

We have conducted a preliminary analysis by varying the AOM parameters in a wide range consistent with the experimental data. This range is

$$e_\sigma^I \quad from \quad 500\ cm^{-1} \quad to \quad 10000\ cm^{-1}$$

$$e_\sigma^{II} \quad from \quad 500\ cm^{-1} \quad to \quad 10000\ cm^{-1}$$

$$e_\sigma^{III} \quad from \quad 500\ cm^{-1} \quad to \quad 10000\ cm^{-1}$$

$$(\frac{e_\pi}{e_\sigma})^I \quad from \quad 0.1 \quad to \quad 0.4$$

$$(\frac{e_\pi}{e_\sigma})^{II} \quad from \quad 0.1 \quad to \quad 0.4$$

$$(\frac{e_\pi}{e_\sigma})^{III} \quad from \quad 0.1 \quad to \quad 0.4$$

Moreover, it has been assumed that the Racah parameters B and C, which in the free ion assume the values 1015 cm^{-1} and 4800 cm^{-1}, respectively, can be lowered as consequence of the ligand field. In Fig.4.2, an example of the influence of the B value on Δ_1 and Δ_2 values has been shown. It is evident that to larger B values, larger values for Δ_1 and Δ_2 correspond.

Some examples of the behaviour of Δ_1 and Δ_2, as function of the AOM parameters, for a fixed geometrical arrangement of the system, are shown in Fig.4.3, (concerning e_σ^I, e_σ^{II} and e_σ^{III}), and in Fig. 4.4 (concerning $(\frac{e_\pi}{e_\sigma})^I$, $(\frac{e_\pi}{e_\sigma})^{II}$ and $(\frac{e_\pi}{e_\sigma})^{III}$).

It can be seen that an increase of the e_σ^I value yields a decrease of the Δ_1 and Δ_2 values; such an effect being more marked for Δ_1. On the contrary, Δ_1 is not affected by changes in the e_σ^{II} and e_σ^{III} values, while the Δ_2 value is lowered according to the sum of the e_σ^{II} and e_σ^{III} values.

Fig.4.4 shows that an increase in the $(\frac{e_\pi}{e_\sigma})^I$ value causes an increase of both Δ_1 and Δ_2 values; moreover, Δ_1 is not influenced by $(\frac{e_\pi}{e_\sigma})^{II}$ and $(\frac{e_\pi}{e_\sigma})^{III}$ which, on

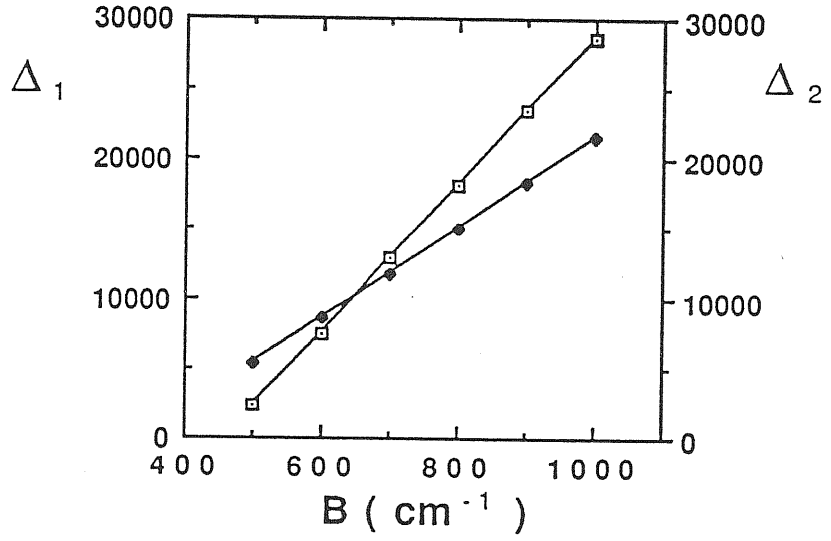

Figure 4.2. Δ_1 and Δ_2 as function of the B parameter. Open symbols refer to Δ_1; full symbols refer to Δ_2. The values of the AOM parameters are: $e_\sigma^I = 10000\ cm^{-1}$, $e_\sigma^{II} = 2000\ cm^{-1}$, $e_\sigma^{III} = 500\ cm^{-1}$, $(\frac{e_\pi}{e_\sigma})^I = 0.1$, $(\frac{e_\pi}{e_\sigma})^{II} = 0.15$; $(\frac{e_\pi}{e_\sigma})^{III} = 0.15$; θ and ϕ are given in Fig.4.1

the contrary, affect the Δ_2 values. Therefore, in general, it should be remarked that the AOM parameters concerning the ligands on the heme–plane can affect both the Δ_1 and Δ_2 parameters, while the AOM parameters associated to ligands in axial position can only affect Δ_2.

In order to reproduce the central values of the crystal field parameter distributions, obtained by the simulation of the EPR spectra (Table 1), the e_σ parameters should be chosen according to the value of the Racah parameters. In what follows, a value of 500 cm^{-1} for B and a value of 2200 cm^{-1} for C, the latter being derived from the condition $C = 4.4\ B$, have been used. These values for B and C fall within the allowed range for iron complexes [49].

Concerning the e_σ parameters, the approximative employed values are: $e_\sigma^I \approx$ 10000 cm^{-1}, $e_\sigma^{II} \approx 2000\ cm^{-1}$ and $e_\sigma^{III} \approx 500\ cm^{-1}$. These values are different from those used for Fe^{2+} [86]; but the higher oxidation state of iron in the present case can make plausible the assumed values. In addition, the value of e_σ^{III} is expected to be smaller than e_σ^{II}, since iron is displaced in the direction

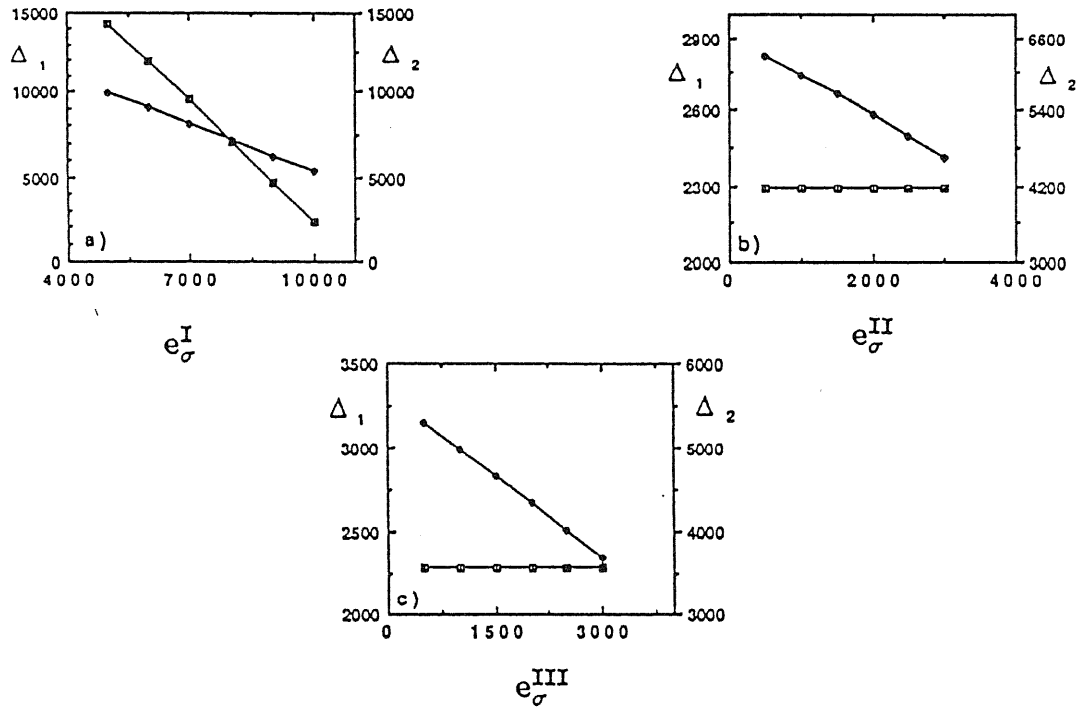

Figure 4.3. Δ_1 and Δ_2 as function of the parameters: e_σ^I (a); e_σ^{II} (b) ; e_σ^{III} (c) are shown. Open symbols refer to Δ_1; full symbols refer to Δ_2. In each figure, all the other AOM parameters are kept fixed; in particular, the following set: $e_\sigma^I = 10000\ cm^{-1}$, $e_\sigma^{II} = 2000\ cm^{-1}$, $e_\sigma^{III} = 500\ cm^{-1}$, $(\frac{e_\pi}{e_\sigma})^I = 0.1$, $(\frac{e_\pi}{e_\sigma})^{II} = 0.15$; $(\frac{e_\pi}{e_\sigma})^{III} = 0.15$ has been employed. Moreover, the values $B = 500\ cm^{-1}$ and $C = 2200\ cm^{-1}$ have been used; θ and ϕ are given in Fig.4.1.

of the fifth ligand. Moreover, in agreement with ref. [86] we have used $(\frac{e_\pi}{e_\sigma})^I = 0.1$ and $(\frac{e_\pi}{e_\sigma})^{II} = (\frac{e_\pi}{e_\sigma})^{III} = 0.15$, as fixed values.

For sake of completeness, some rhombicity effect should be considered. In our simulation, a rhombicity distortion, derived from the splitting of the ξ and η levels, has been introduced through the γ parameter (see Fig. 2.7). Such a splitting can be reproduced, in the AOM approach, both by considering a small distortion of the porphyrin core [87] and by introducing small slidings of the porphyrin with respect the metal ion [41]. However, since this contribute is much smaller than the other ones, it has not explicitly introduced in our calculations.

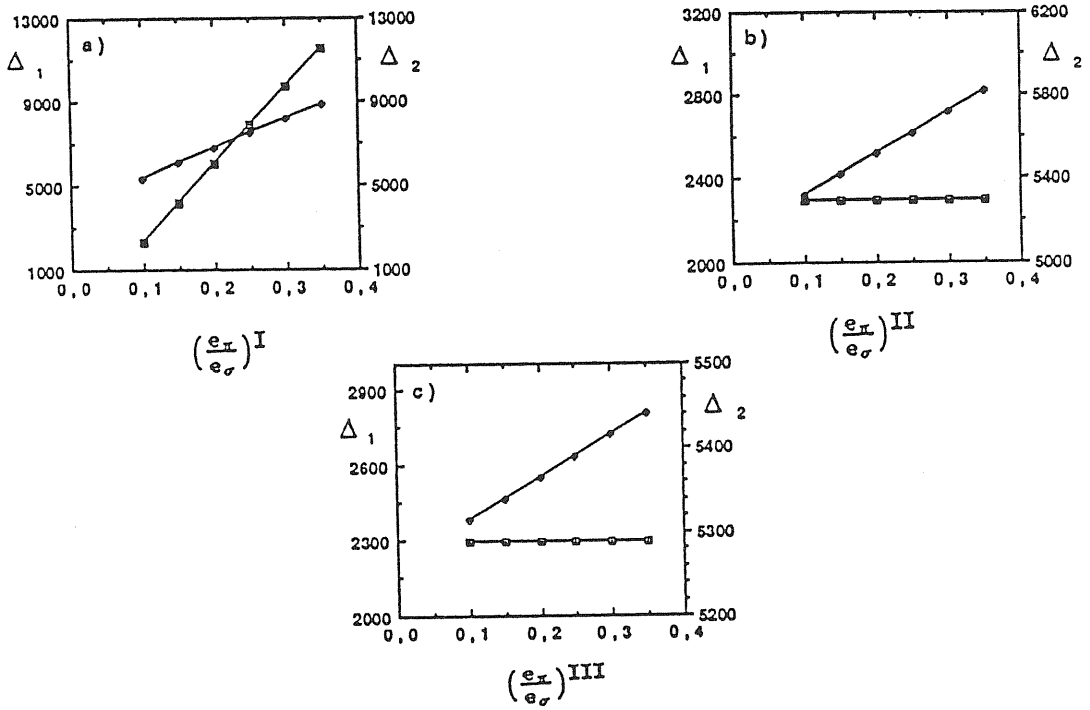

Figure 4.4. Δ_1 and Δ_2 as function of the parameters: $(\frac{e_\pi}{e_\sigma})^I$ (a); $(\frac{e_\pi}{e_\sigma})^{II}$ (b); $(\frac{e_\pi}{e_\sigma})^{III}$ (c) are shown. Open symbols refer to Δ_1; full symbols refer to Δ_2. In each figure, all the other AOM parameters are kept fixed; in particular, the following set: $e_\sigma^I = 10000\ cm^{-1}$, $e_\sigma^{II} = 2000\ cm^{-1}$, $e_\sigma^{III} = 500\ cm^{-1}$, $(\frac{e_\pi}{e_\sigma})^I = 0.1$, $(\frac{e_\pi}{e_\sigma})^{II} = 0.15$; $(\frac{e_\pi}{e_\sigma})^{III} = 0.15$ has been employed. Moreover, the values $B = 500\ cm^{-1}$ and $C = 2200\ cm^{-1}$ have been used; θ and ϕ are those given in Fig.4.1.

4.2.1 A model to interpret the EPR results

The analysis shown in last section will be the starting point to interpret the results concerning the crystal field parameter distributions of Chapter 3.

At first, we consider the central values, Δ_1^o and Δ_2^o of the distributions corresponding to Mb samples in different conditions. The observed variations of these parameters could be mainly attributed to changes occurring to ligands in both the fifth and the sixth positions, since ligands on the heme–plane are assumed to be very small affected by changes in the protein solutions. Accordingly, we have assumed that the e_σ^I values are equal for all the Mb samples and we have determined the mean values for the iron–porphyrin displacement

in order to exactly reproduce the Δ_1^o value. Then, the e_σ^{II} and e_σ^{III} values have been adjusted to obtain the corresponding value for Δ_2^o.

TABLE 3 The values of the parameters, employed in the AOM approach, are reported. a_o is the mean value for the iron–porphyrin displacement. e_σ^I is the AOM parameter concerning with the ligands on the heme–plane; e_σ^{II} and e_σ^{III} are the AOM parameters concerning with the fifth ligand and the sixth ligand, respectively. For abbreviations see section 3.1.

SAMPLE	$a_o(\AA)$	$e_\sigma^I\ (cm^{-1})$	$(e_\sigma^{II} + e_\sigma^{III})\ (cm^{-1})$
Mb (Fast)	0.400	10010.	1954.
Mb+Gly (Fast)	0.394	10010.	2160.
Mb+EthGly (Fast)	0.398	10010.	2460.
Mb+Sucro (Fast)	0.390	10010.	1872.
Mb+Meth (Fast)	0.387	10010.	1748.
Mb+Eth (Fast)	0.388	10010.	2100.
Mb pH =5.6 (Fast)	0.396	10010.	2440.
Mb pH=9 (Fast)	0.390	10010.	1775.
Mb (Slow)	0.398	10010.	1920.
Mb+Gly (Fast)	0.398	10010.	2473.

In Table 3, the mean values of the iron–porphyrin displacement, a_o, and the values of the AOM parameters e_σ^I and $e_\sigma^{II} + e_\sigma^{III}$ which have allowed us to reproduce the values of Δ_1^o and Δ_2^o values are reported for all the analyzed Mb samples.

By looking at the a_o values, it comes out that no large changes occur in the different Mb samples. The most significant changes concern Mb samples in the presence of small amount of methanol and ethanol, in which a decrease of a_o,

with respect to that of pure Mb solutions, of about 3% is observed. In all the other cases, changes smaller than 1% occur.

Concerning the $e_\sigma^{II} + e_\sigma^{III}$ values, the most significant deviations from the value of pure Mb solutions correspond to samples in presence of ethylene glycol, in which an increase of 26% is registered, and to samples at pH=5.6, in which this parameter increases of 25%. Moreover, $e_\sigma^{II} + e_\sigma^{III}$ decreases of 10% in solutions with methanol, and of 9% in solutions at pH=9. In this connection, it should be noted that, since Δ_2 is dependent on the sum of $e_\sigma^{II} + e_\sigma^{III}$, it is not possible to single out the contribution of each of the latter.

We consider, now, the spread in the Δ_1 and Δ_2 values. The distributions in Δ_1 and Δ_2, reflect the degree of heterogeneity of the microenvironment around the metal ion and they should be reproduced by distributing some structural parameters (like the angles θ and ϕ and the iron–ligand distance) which characterize the heme–complex. On the other hand, we know that the presence of CS is responsible for such a heterogeneity [12]. The question that can be risen is how the parameters which characterize the heme–structure can be affected by the presence of CS distribution. The fact that protein molecules may assume different CS yields, as it has been observed by X–ray diffraction [16,40], a significant mean–square displacement of each amino–acid residue (see Chapter 1). Therefore, it could be expected that the ligand in the fifth position, which is directly bound to the protein chain and senses the effects induced by the presence of CS distribution, can, on turn, exercise some effect on the metal ion and induce some changes in the heme–group structure. In this context, it should be observed that proximal histidine shows a mean square displacement, $< x^2 >$, of about $0.10 \AA^2$; in particular, for metMb (see Fig.1.3), a value of $0.07 \AA^2$ from extrapolation to 0 K, and $0.12 \AA^2$ from interpolation to 300 K [40]

are observed. Therefore, it could be assumed that such a disorder in the proximal histidine position may be responsible for the modulation of the strengths exercised, from nitrogen of imidazole, on the iron. On such a ground, it is reasonable to assume that, as consequence of the presence of different positions of the proximal histidine, the iron is forced to change its position with respect to the heme–plane. In other words, it can be supposed that the iron can follow the histidine displacements, and then, it changes its geometrical arrangement with respect to the other ligands. On the other hand, there are many experimental evidences supporting the fact that the iron position, in ferrous deoxy Mb, is distributed [16,48] [88,89]. It is plausible that also in high spin ferric Mb samples, the distance of iron from the heme–plane is distributed according to the presence biomolecule structures in many different CS.

In such a context, we have tried to numerically reproduce Δ_1 and Δ_2 distributions by introducing a distribution in the iron position.

The model employed to interpret the results extracted by simulations of the EPR spectra can be summarized as follows. Because of the presence of CS distribution, proximal histidine forces the iron to assume different positions with respect to the heme–plane, this fact implies a change in the geometry of the system, *i.e.* in the values of the θ and ϕ angles and in the length of the iron–ligand bonds. In this context, it can be observed that, since an increase of the bond–length causes a lowering of the angular overlap integral S, a correction, depending on the iron–porphyrin displacement, should be introduced in the AOM approach. A correction has been introduced, in agreement with ref. [90], alos by taking into account that the dependence on the bond–length is more marked for the e_π parameter.

In general, there is not any reason for which the iron should be symmetrically

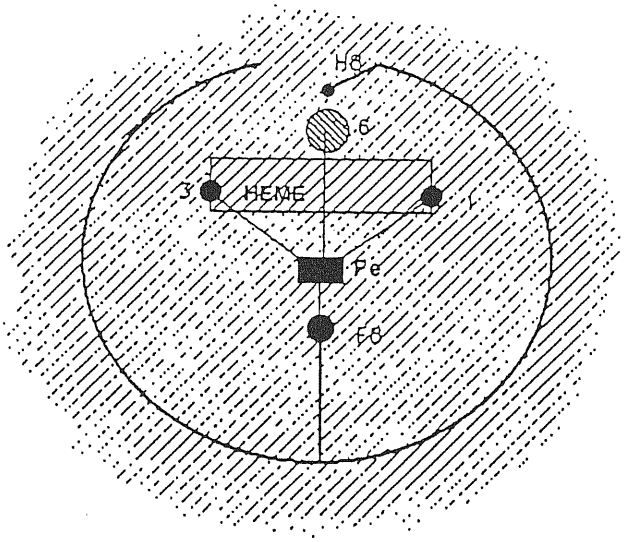

Figure 4.5. A schematic figure showing the coupling between the iron and the protein matrix through the action of the proximal histidine.

distributed around the mean value. Indeed, a sort of asymmetry could be expected for the iron displacement. To encompasses such a possibility, the distribution has been assumed to be given by a gaussian characterized by two variances: one for the negative displacements and one for the positive ones; where negative means that the iron is brought near the iron, and positive that it is taken away. Starting from the Δ_1 and Δ_2 distributions, a fit has been performed in order to extract the variances of the iron–porphyrin displacement.

4.3 Results

The results obtained by the application of the AOM to the EPR results, shown in Table 1, are reported in Table 4.

Fig.4.5 shows an example of the agreement between the Δ_1 and Δ_2 distributions, as derived from the analytical expression of gaussians with central values and variances taken from Table 1, and those obtained by the fit based on the

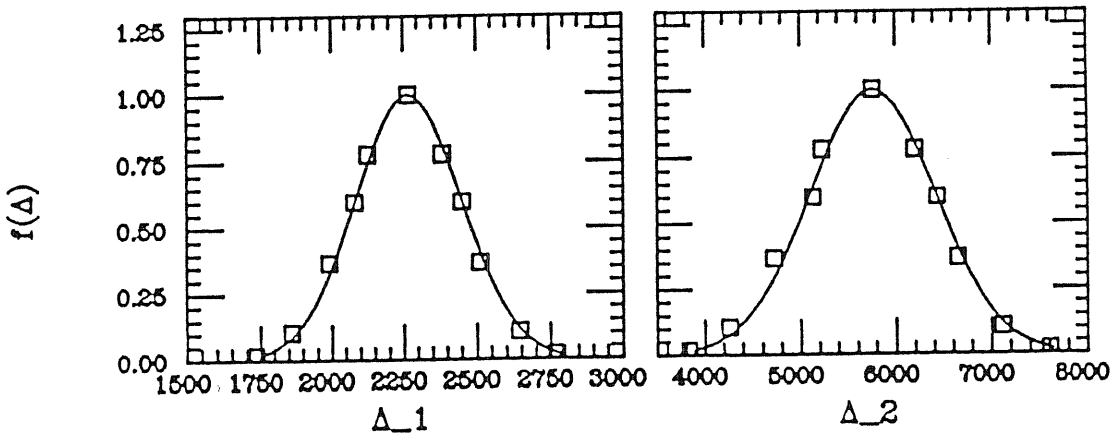

Figure 4.6. The gaussian distributions, $f(\Delta)$, of the crystal field parameters Δ_1 and Δ_2 (continuous lines) and the fit (square symbols), extracted by the AOM approach, concerning with pure fast cooled Mb samples at pH = 6.7, are shown.

model presented in the last section. The σ_a value concerning with pure Mb solutions ($0.0575\mathring{A}$) is to be compared with that of ferrous deoxy Mb. In this case, different experimental techniques provided different results: σ_a should fall within the interval $0.07\ \mathring{A} - 0.3\ \mathring{A}$ [16,48] [88,89]. The smaller value, for ferric Mb, can be justified by both the higher oxidation state for the iron and the presence of the weak sixth ligand.

The values of column 4 in Table 4 point out that a significant asymmetry is present in the distribution of the iron–porphyrin displacement. In particular, the iron prefers to approach to the heme plane rather than to take away from it. Even if no experimental evidence can be provided, it could be assumed reasonable that the ligands on the heme–plane, in connection with the action of the 6th ligand, might prevent the iron to perform large displacements to the proximal side.

Addition of large amount of glycerol, ethylene glycol and sucrose to Mb solutions, which, as it has been seen in Chapter 3, causes a narrowing of the crystal field parameter distributions, results in a significant decrease in the σ_a value.

TABLE 4 The values of root of variances for the gaussian distributions of the iron–porphyrin displacement, a, as extracted from the results in Table 1 by a fit based on the AOM approach, are presented. The mean value a_o of the distributions has been shown in Table 3. σ_a^- concerns with the approach of iron to the heme–plane; σ_a^+ concerns with the departure of iron from the heme–plane; the mean value, $\sigma_a = \frac{\sigma_a^- + \sigma_a^+}{2}$, and the ratio, $\frac{\sigma_a^-}{\sigma_a^+}$, are also shown. In each case, the goodness of the fit has been confirmed by the χ^2 test. For abbreviations see section 3.1.

SAMPLE	$\sigma_a(\AA)$	$\sigma_a^-(\AA)$	$\sigma_a^+(\AA)$	$\frac{\sigma_a^-}{\sigma_a^+}$
Mb (Fast)	0.0575	0.0646	0.0504	1.28
Mb+Gly (Fast)	0.0325	0.0349	0.0302	1.16
Mb+EthGly (Fast)	0.0374	0.0404	0.0343	1.18
Mb+Sucro (Fast)	0.0385	0.0423	0.0346	1.22
Mb+Meth (Fast)	0.0522	0.0583	0.0461	1.26
Mb+Eth (Fast)	0.0500	0.0557	0.0443	1.26
Mb pH=5.6 (Fast)	0.0564	0.0632	0.0496	1.27
Mb pH =9 (Fast)	0.0540	0.0599	0.0481	1.25
Mb (Slow)	0.0563	0.028	0.0498	1.26
Mb+Gly (Slow)	0.0308	0.0326	0.0290	1.12

This effect is more marked for samples with added glycerol, in which σ_a^- is lowered of 46% and σ_a^+ of 40%; while for ethylene and sucrose, σ_a^- is reduced of 37% and 34%, respectively; and σ_a^+ is reduced of 32% and of 31%. The ratio $\frac{\sigma_a^-}{\sigma_a^+}$ appears to be reduced as compared with that of pure Mb indicating a more symmetrical behaviour for the spread of the iron position.

Addition of small quantities of methanol and ethanol to pure Mb solutions causes a lowering in both σ_a^- and σ_a^+values; the effect being more marked for ethanol. In particular, σ_a^- is decreased of 10% and 14% for samples with

methanol and ethanol, respectively; while σ_a^+ is reduced of 9% for samples with added methanol and of 12% for samples with added ethanol. The ratio $\frac{\sigma_a^-}{\sigma_a^+}$ is slightly affected by the addition of these alcohols.

The lowering pH affects little the σ_a^- and σ_a^+ values: both of them decrease of about 2%. More significant changes are, on the contrary, observed by increasing the pH value: σ_a^- is decreased of 7% and σ_a^+ of 5%. The ratio $\frac{\sigma_a^-}{\sigma_a^+}$ is not much affected by pH changes, small decreases being observed in both the cases.

For pure Mb solutions, σ_a^- is reduced of 3% and σ_a^+ of the 1% when the samples are submitted to slow cooling rate. In samples containing glycerol, slow cooling rate causes a reduction of σ_a^- of 7% and of σ_a^+ of 4%. Moreover, a small decreasing in the asymmetry of the iron distribution is observed.

4.4 Discussion

The distributions of the crystal field parameters Δ_1 and Δ_2, extracted by simulation of the EPR spectra of high spin ferric Mb solutions in different conditions, are indicative of a significant heterogeneity in the microenvironment of the iron. The AOM approach allowed us to rationalize this heterogeneity in terms of a distribution of the iron–porphyrin displacement. Such a displacement can be modulated by the proximal histidine which on turn may be determined by the particular conformational substate assumed by the protein. In other words, the proximal histidine, frozen in different position being affected by the presence of CS distribution, forces the iron to assume different arrangements within the heme–complex.

It should be noted that, since different positions for the iron, with respect the heme–plane, are involved in the ligand and unligand state of the protein

[80], the iron–porphyrin displacement is a parameter directly involved in the biological functionality [48]. On such a ground, our results from EPR and AOM approaches, are discussed in connection also with some results from models of rebinding kinetics.

It should be moreover remarked that the iron–porphyrin displacement is a parameter which can be analyzed by means of other spectroscopic investigations; *e.g.* band III, a charge–transfert transition involving iron and porphyrin states, occurring in ferrous deoxy Mb, could be employed to extract information about the iron position [30].

4.4.1 Connection with rebinding models

Several theoretical approaches have been developed in order to explain rebinding kinetics, as studied by flash photolysis experiments, by means of models taking into account the coupling between protein dynamics and biological functionality [46,47] [48,91]. In the Srajer *et al.* model [48], which is a development of the Agmon and Hopfield [46] and of Bowne and Young [47] models, the ensemble of Mb molecules is described by three coordinates: r, Q and x; r is the reaction coordinate corresponding to the distance Fe–ligand (CO); Q, the iron–porphyrin coordinate, is equal to the displacement of the iron from the porphyrin–plane; finally, x, the internal protein coordinate, takes into account the fact that protein molecules in the solution are arranged in many different CS. The peculiar difference of this model, with respect to the Agmon–Hopfield and the Young–Browne models, is that the distance of iron from the heme–plane is assumed to be a parameter essential to treat rebinding processes.

Even if the model deals with Mb in the ferrous form, the extension to the ferric

form, for the particular aspects to which we are interested, can be performed without substantial modifications.

The probability distribution of the internal coordinate x can be expressed, by means of the quasiharmonic approximation [92], as

$$P(x,T_o) = \left[\frac{f}{2\pi k_B T_o}\right]^{\frac{1}{2}} e^{-\frac{f(x-x_o)^2}{2k_B T_o}} \tag{46}$$

where k_B is the Boltzmann constant and x_o is the most probable value for the internal protein coordinate depending on the protein state; for the temperature T_o, it is

$$T_o = T \quad if \quad T > T_f \tag{47}$$

$$T_o = T_f \quad if \quad T \leq T_f \tag{48}$$

where T is the current temperature of the sample and T_f is the freezing temperature, *i.e.* the temperature below which transitions among CS cannot occur and the protein coordinate x is frozen. The force constant f takes into account for both protein–solvent and protein–protein interactions.

At low temperature, the ligand, after the rupturing of its bond with the iron, passes to the heme–pocket from which it can rebind to the iron. The barrier that the ligand must overcome to binding to the metal ion, is assumed to be

$$H(a) = H_D + \frac{1}{2}Ka^2 \tag{49}$$

where H_D, the distal pocket work, takes into account the overall effects involved in the distal part of the protein, (*i.e.* the side of the distal histidine). The second term in eq.(49), to which we are particularly interested, takes into account that iron, after the breaking of the binding and having relaxed away from the heme–plane to the proximal histidine site, is forced to move back to the heme–plane. The force involved in this process has been considered proportional to the

distance a that iron must cover in order to bind the ligand. Some experimental confirmations, for the dependence of H from a, come from kinetic hole burning measurements on band III in photodissociated MbCO [30].

Since the protein matrix is directly bound to the metal ion, through the proximal histidine, the displacement a of the iron is expected to be coupled to the protein structure; then, to each substate of the protein can correspond a mean distance a. In the Srajer model, this coupling is assumed to be expressed as

$$a(x) = a_o + \alpha(x - x_o) \tag{50}$$

where a_o is the average value for the iron–porphyrin displacement and α is the coupling parameter between iron and protein matrix. In general, it should be expected a more complex dependence for $a(x)$ from x; however, the independence of α from x could be assumed, at this level of approximation, to be reasonable.

From eq.(46) and from eq.(50), it can be derived that the distance a is distributed in a gaussian way with the variance given by

$$\sigma_a^2 = \frac{\alpha^2 k_B T_f}{f} \tag{51}$$

By means of this expression, it is possible to put into relation the spread of the a parameter to the f constant associated to the distribution of the internal protein coordinate.

We will try to use the above discussed model to our results. First of all, we have found that the displacement of the iron from the heme–plane is distributed in an asymmetrical way with respect to the equilibrium position. This fact could be interpreted by assuming that two different coupling parameters should be introduced: one for the approach of the iron to the heme–plane (α^-), and one

for the departure from heme–plane (α^+). Now, however, a single parameter α, derived from the mean value σ_a, is employed.

From eq.(51), it can be derived the expression

$$\frac{f}{\alpha^2} = \frac{k_B T_f}{\sigma_a^2} \tag{52}$$

From the values reported in Table 4, and known the values of the freezing temperature T_f, the values for $\frac{f}{\alpha^2}$ for all the analyzed Mb samples can be calculated through eq.(52). The coupling between the protein matrix and the iron, expressed by the α constant, is associated to an intrinsic property of the protein molecule; then, it can be assumed to be independent on the conditions to which the protein is submitted. On the contrary, the f constant, which is directly connected to the distribution of the internal protein coordinate x, is expected to be strongly dependent on the external conditions, *i.e.* solvent composition, pH etc. Therefore, if the α parameter is assumed to be the same for all the analyzed Mb samples, from the values of $\frac{f}{\alpha^2}$, some information concerning the distribution of the internal protein coordinate x, as induced by external agents could be extracted.

We introduce now a new parameter that could allow us to estimate the heterogeneity of the system. Let us consider the expression

$$F(f, T_o) = \int_{-X_M}^{X_M} P(x, T_o) dx \tag{53}$$

where $P(x, T_o)$ is given by eq.(46) with $x_o = 0$.

F is the fraction of molecules, at the temperature T_o, which have an internal coordinate x between $-X_M$ and X_M. Since f is unknown, we introduce a new variable $y = \alpha x$, so that eq.(53) becomes

$$F(\frac{f}{\alpha^2}, T_o) = \int_{-Y_M}^{Y_M} \left[\frac{f}{2\pi\alpha^2 k_B T_o}\right]^{\frac{1}{2}} e^{-\frac{f(y-y_o)^2}{2\alpha^2 k_B T_o}} dy \tag{54}$$

By inserting in eq.(54) the $\frac{f}{\alpha^2}$ value, and provided that T_o and F are known, $Y_M(T_o, F)$ can be calculated. This quantity can be assumed to represent an estimate of the heterogeneity of the system. Actually, if at the temperature T_o, the same fraction F of molecules is distributed over a wider protein coordinate range, an increased heterogeneity is then present in the system. In other words, $Y_M(T_o, F)$ gives some information about the number of protein molecules which have different internal coordinates, *i.e.* different CS, at the temperature T_o. The above mentioned results are summarized in Table 5.

TABLE 5 The values of the freezing temperature T_f, of $\frac{f}{\alpha^2}$, derived from eq.(52) by using the mean value for σ_a, and of Y_M, extracted by eq.(54), are reported. The freezing temperatures that are not referenced should be considered as indicative, since experimental data are not available. $Y_M(T, F)$, has been obtained with T = 300 K for fast cooled samples, and with T equal the corresponding freezing temperature for slowly cooled samples. For abbreviations see section 3.1.

SAMPLE	$T_f(K)$	$\frac{f}{\alpha^2}(\frac{kJ}{mol\AA})$	$Y_M(\AA)$
Mb (Fast)	220[46]	553.	3.50
Mb+Gly (Fast)	180[22]	1417.	2.19
Mb+EthGly (Fast)	160[22]	951.	2.67
Mb+Sucro (Fast)	220	1237.	2.34
Mb+Meth (Fast)	220	671.	3.18
Mb+Eth (Fast)	220	732.	3.04
Mb pH=5.6 (Fast)	220	575.	3.43
Mb pH =9 (Fast)	220	627	3.29
Mb (Slow)	220[46]	577.	2.93
Mb+Gly (Slow)	180[22]	1578.	1.61

It can be noted that addition of large amount of glycerol, ethylene glycol and sucrose causes a large increase of the f parameter and also a decrease of the parameter Y_M. These results point out that addition of these solvents results into a significant decrease in the heterogeneity of the system. Because of the increase of the force constant f, as induced by these added solvents, the increase of solvent–protein interaction should considered as responsible for such an effect. Addition of small amount of methanol and ethanol results in a quite large increase of f and in a decrease of Y_M values; moreover, such an effect is more marked for samples in presence of ethanol.

The f and Y_M values seem to be not much affected both by increase and by decrease of the pH value; in any case, higher pH values seem to be more effective in narrowing the CS distribution.

Finally, it should be noted that slow cooling rate yields a small increase of the f value in pure Mb solutions, and a more significant increase in solutions with added glycerol. On the contrary, in both cases, it is observed a significant reduction of the parameter related to the heterogeneity (Y_M). The fact that the f parameter is affected by the cooling procedure means that a modification in the system can be performed by acting on the cooling procedure. In other words, the intrinsic ensemble of CS can be modified by the cooling rate. The significant decrease of the value of Y_M is to be attributed to the fact that it has been assumed that the system can equilibrate until the freezing temperature is reached. This assumption requires some discussion and it will be done in the next section.

4.4.2 Cooling rate effects

Small modifications have been obtained in the spread of the iron–porphyrin displacement as induced by slow cooling rate. In the hypothesis that such an effect could be attributed to a modification of the CS distribution, different possible causes should be taken into account.

First of all, the dependence of distributions on the cooling rate could be due to a modification of hydration water as induced by the cooling process. In this context, it should be noted that calorimetric measurements have shown that the amorphous character of the adsorbed water in Mb displays a significant dependence on the cooling rate [36,39]. On such a ground and with the additional support of dielectric results [93], it has been hypothesized that protein dynamics is coupled to the water dynamics which, in turn, is modulated by the kinetics of the H–bond network. In such a framework, the protein CS distribution is seen as induced by the multiplicity of the water states, (multiplicity of the water cluster dimensions). Then, a sufficiently slow cooling rate, which is able to reduce such an heterogeneity (leading to a less amorphous character), would in turn reduce the multiplicity of the CS. In other words, it could yield a decrease in the number of accessible CS and then a narrowing of the CS distribution. The presence of an effect which is able to modify the intrinsic CS distribution can be also seen through the changes in the f value as induced by different cooling rates. In fact, the modifications in the force constant f mean that the distribution of internal protein coordinate can be really affected by cooling procedures.

Furthermore, a sort of "condensation" might take place in the molecules populating the CS distribution. A rapid cooling, probably, does not allow the system to thermally equilibrate during the temperature decreasing. As a consequence, it could happen that the CS landscape of the final state practically coincides

with that corresponding to the initial state; in other words, a sort of photography has been performed on the system. On the contrary, we can imagine that, if the temperature is gradually decreased, the system may reach the thermal equilibrium until the freezing-temperature T_f and the protein molecules could condensate in those CS with lower energy. This means that transitions among CS can take place during the lowering of the temperature, however, not all the transitions are allowed. The final state should correspond to the state at which transitions among CS cannot be anymore performed, *i.e.* at the freezing temperature of the system. In other words, the CS distribution may be affected by the cooling rate as a consequence of the different partition of the molecules with respect to the CS energy distribution. In order to quantify this effect, let us consider the expression

$$C(T_1, T_2, F) = \frac{Y_M(T_1, F) - Y_M(T_2, F)}{Y_M(T_1, F)} \tag{55}$$

where the temperatures T_1 and T_2 are both higher (or equal) than the freezing–temperature and satisfy the condition $T_1 > T_2$. $Y_M(T, F)$ is derived from eq.(54) for a given fraction of molecules. As we have already said, $Y_M(T, F)$ can be assumed to satisfactorily represent the heterogeneity of the system. We have put T_1 equal to the room temperature, and T_2 to the freezing–temperature depending on the solvent composition of the system. The parameter $C(T_1, T_2, F)$ indicates in which way a condensation effect could affect our samples.

For pure Mb, by employing the f constant related to fast cooled samples, it results C = 0.14. This value points out that a significant reduction in the heterogeneity of the system could be induced by acting on the cooling rate. For Mb samples in presence of glycerol, it is C = 0.23; this larger value of C, with respect that of pure Mb samples, could be attributed to a decrease of the freezing temperature as induced by the presence of glycerol, so the system is

allowed to follow the thermal equilibrium at a lower temperature. This fact would imply that a slow cooling rate could be more effective in determining a condensation in samples containing glycerol with respect to samples without glycerol. The values for the C parameter should be compared with variations of the parameters extracted by EPR spectra (principally the spread of Δ_2 and a) as induced by slow cooling rate. In general, these variations are about 2% and 6% for samples without and with added glycerol, respectively. Then, the observed changes are smaller than those expected. This fact can be explained by taking into account that it is probably that slow cooling rate cannot be completely efficient to yield a condensation of molecules in the states with lower energy. In other words, it could happen that some constrains on the protein solution prevent the system to reach a complete condensation. However, it should be noted that the trend in presence and in absence of glycerol is confirmed.

Anyway, it should be remarked that the presence of other effects which could be superimposed to these ones cannot be ruled out.

To sum up, the results point out that, on one hand, a slow cooling rate can affect the population in the CS energy distribution by lowering the heterogeneity of the system; on the other hand, the lowering of the freezing–temperature of system, due to the presence of glycerol, can be adduced as responsible for the magnification of the effect induced by the slow cooling rate.

4.4.3 Effects induced by solvent composition

In general, addition of glycerol, ethylene glycol and sucrose to Mb solutions results into a significant decrease in the spread of the iron–porphyrin displacement. Since iron is not directly exposed to the external solvent, modifications

induced by addition of these solvents should be attributed to a reduction in the heterogeneity of the strengths exercised by the proximal histidine onto the metal ion. In other words, proximal histidine, directly bound to the protein matrix, undergoes, in the presence of these solvents, to weaker perturbations from other parts of the protein, affecting in a less significant way the metal ion position. These results can be directly interpreted in terms of a reduction in the heterogeneity in the CS distribution as induced by addition of these solvents. Moreover, the observed increase of the force constant f concerning with the distribution of internal protein coordinate x, points out that these effects could be attributed to an increase of the strengths related to the protein–solvent interaction, and that a sort of stabilization is induced in the protein molecule [94]. It should be remarked that addition of glycerol, ethylene glycol and sucrose causes an increases of the viscosity of medium and therefore, these changes might be responsible for a decrease of the protein mobility leading to a damping of the protein motions. Moreover, it has been observed that glycerol, which is preferentially excluded from the domain of protein (first hydration shell) [94,95], causes a decrease in the hydrogen–bond–rupturing capacity of the medium [95] and then stabilizes the protein structure. Such a constraint on the dynamics of the solvent, could be responsible for the decreased number of accessible CS and for the decrease in the structural heterogeneity of the protein molecules observed in the presence of glycerol. A similar mechanism might be operative for what concerns protein solutions in presence of ethylene glycol which shows chemico–physical properties similar to glycerol. Moreover, a similar constraint on the protein dynamics can be induced by sucrose which, however, is known to stabilize the protein structure through an increase of the water surface tension [96,97] which, on the contrary, is slightly decreased by the presence of glycerol.

To asses which one of these molecular mechanisms is operative would requires a deeper investigation but, in any case, it should be remarked that modifications in the solvent properties might affect the CS distribution. In this context, it should be noted that data from rebinding kinetics experiments performed in presence of glycerol or ethylene glycol, should be discussed in close connection with these results.

4.4.4 Effects induced by addition of small amount of alcohols

Since the decrease in the σ_a parameter is induced by addition of methanol and ethanol in quite limited quantities, at which the intrinsic CS distribution of the protein is not substantially modified, it should be attributed to some kind of modifications, independent from CS distribution, in the microenvironment around the metal ion.

As we have already mentioned, methanol, and probably ethanol, are directly bound to the metal ion [79], and so they are able to affect the crystal field parameters. From Table 3, it is evident a reduction of the mean value of the iron–porphyrin displacement for Mb samples in presence of these alcohols. This effect could be reasonably explained by admitting that a stronger force sensed by the iron through the action of the sixth ligand. This stronger interaction would hold the iron closer, in average, to the heme–plane and, in the mean time, would restrict the distribution of possible a corresponding to different CS.

4.4.5 Effects induced by pH changes

Changes of the pH value with respect the physiological value, result into a quite small modification of the spread of the iron–porphyrin displacement. These

results seem to point out that that no drastic changes in the protein structures occur. In general, it should be noted that the pH value can affect the protein solution in different ways; on one hand, it can affect the protein structure, e.g. through changes of the electrical charge of amino–acid residues; on the other hand, it can affect the solvent properties through modifications of the network of hydrogen–bonds. Therefore, the CS distribution could be affected by changes in the pH value both by means of changes of the overall protein structure, and by the modifications in the hydration water. It has been observed, by infrared spectroscopy, that pH value affects the CS distribution in MbCO solutions [3]; in particular, the distribution of the CO positions, with respect to the heme–plane, results to be significantly modified by lowering of the pH value. Our results, on the contrary, show that in high spin Mb the most significant modifications occur solutions at pH 9. However, in general, the observed effect on the CS distribution as induced by pH changes seem not much remarkable.

Conclusions

It should be pointed out that, owing to its high sensitivity in detecting microenvironmental fluctuations around the paramagnetic probes, EPR spectroscopy is a rewarding tool to investigate structural and dynamical properties of proteins.

The EPR spectra of high spin ferric Mb samples in different conditions have been carefully analyzed in terms of two crystal field parameter distributions. This analysis has allowed us to extract detailed information about the effects induced by added solvents, pH changes and different cooling rates on the environment around the metal ion. The presence of the crystal field parameter distributions can be directly put into relation to the existence of CS distribution.

An approach based on the AOM has allowed us to correlate the crystal field parameters with the geometrical arrangement of heme–group. The crystal field parameter distributions can be moreover interpreted as due to the presence of a distribution in the iron–porphyrin displacement. In particular, the iron position can be seen as modulated by the proximal histidine which, as consequence of the presence of CS distribution, may assume slightly different positions. In other words, the existence of CS distribution directly reflects, through the action of the proximal histidine, onto the metal ion which can be found in different arrangements within the heme–group. Therefore, the iron can be considered

a reporter particularly suitable to the study of CS distribution in Mb and, moreover, to the analysis of the agents that could affect the CS distribution.

On the other hand, it can be observed that, since the distance of iron from the heme–plane is a parameter directly involved into the functional role, these results should be analyzed in connection with the biological functionality of the protein. Changes in the CS distribution resulting into modifications of distribution of the iron–porphyrin displacement, could consequently affect the dynamical aspects of the biological functionality of the protein.

In this context, it should be remarked that glycerol and ethylene glycol, widely employed to perform flash photolysis experiments by optical spectroscopy, can significantly affect the CS distribution. Therefore, as long as the ferric heme proteins mimic the ferrous heme proteins, at least for their CS landscape, EPR constitutes a complementary technique to optical spectroscopy in order to study the CS energy distribution. In particular, since it does not require any added solvent and, at the same time, it can be performed in the presence of different solvents, it results particularly suitable to analyze the solvent–induced effects on the CS distribution.

Bibliography

[1] Frauenfelder, H., Parak, F., Young, R.D.: Ann. Rev. Biophys. Biophys. Chem. **17** 451–479 (1988) *and refs. therein.*

[2] Goldanskii, V.I. and Krupyanskii, Y.F.: Quart. Rev. Biophys. **22** 39–92 (1989).

[3] Hong, M.K., Braunstein, D., Cowen, B.R., Frauenfelder, H., Iben, I.E.T., Mourant, J.R., Ormos, P., Scholl, R., Schulte, P.J., Steinbach, P.J., Xie, A.H., Young, R.D.: Biophys. J. **58** 429–436 (1990).

[4] Di Iorio, E.E., Hiltpold, U.R., Filipovic, D., Winterhalter, K.H., Gratton, E., Vitrano, E., Cupane, A., Leone, M., Cordone, L.: Biophys. J. **59** 742–754 (1991).

[5] Frauenfelder, H., Alberding, N.A., Ansari, A., Braunstein, D., Cowen, B.R., Hong, M.K., Iben, I.E.T., Johnson, J.B., Luck,S., Marden,M.C., Mourant, J.R., Ormos, P., Reinisch, L., Scholl,R., Schulte, A., Shyamsunder, E., Sorensen, L.B., Steinback, P.J., Xie, A. H., Young, R.D., Yue, K.T.: J. Phys. Chem. **94** 1024–1037 (1990).

[6] Ansari, A., Berendzen, J., Bowne, S.F., Frauenfelder, H., Iben, I.E.T., Sauke, T.B., Shyamsunder, E., Young, R.D.: PNAS USA **82** 5000–5004 (1985).

[7] Frauenfelder, H., Steinbach, P.J., Young, R.D.: Chemica Scripta **29A** 145–

150 (1989).

[8] Cordone, L., Cupane, A., Fornili, S.L.: Biopolymers **22** 1677–1696 (1983).

[9] Agmon, N.: J. Phys. Chem. **94** 2959–2936 (1990).

[10] Ansari, A., Berendzen, J., Braunstein, D., Cowen, B.R., Frauenfelder, H., Hong, M.K., Iben, I.E.T., Johnson, J.B., Ormos, P., Sauke, T.B., Scholl, R., Schulte, A., Steinback, P.J., Vittitow, J., Young, R.D.: Biophys. Chem **26** 337–355 (1987).

[11] Bacci, M. and Cannistraro, S.: Appl. Mag. Res. **1** 369–378 (1990).

[12] Bizzarri, A.R. and Cannistraro, S.: Biophys. Chem. (1991) in press.

[13] Levy, R.M. and Karplus, M.: Biopolymers **18** 2465–2495 (1979).

[14] Bialek, W. and Goldstein, R.F.: Biophys. J. **48** 1027–1044 (1985).

[15] Elber, R. and Karplus, M.: Science **235** 318–321 (1987).

[16] Frauenfelder, H., Petsko, G.A., Tsernoglou, D.: Nature **280** 558–563 (1979).

[17] Parak, F. and Reinisch, L.: Methods Enzymol. **131** 568–632 (1986).

[18] Cusack, S. and Doster, W.: Biophys. J. **58** 243–251 (1990).

[19] Smith, J.C.: Q. Rev. Biophys. **24** 227–291 (1991).

[20] Kubo, R.: Rep. Prog. Phys. **29** 225–284 (1966).

[21] Frauenfelder, H. in: "Proteins and Glasses" (Luscher,E., Fritsch, G., Jacucci, G., eds.) pp.3–18, Amorphous and Liquids Materials, NATO series, Martinus Nijhoff Publishers, Dordrecht (1987).

[22] Iben, I.E.T., Braunstein, D., Doster, W., Frauenfelder, H., Hong, M.K., Johnson, J.B., Luck, S., Ormos, P., Schulte, A., Steinbach, P.J., Xie, A.H., Young, R.D.: Phys. Rev. Lett. **62** 1916–1919 (1989).

[23] Stein, D.L.: PNAS USA **82** 3670–3672 (1985).

[24] Bryngelson, J.D. and Wolynes, P.G.: PNAS **84** 7524 –7528 (1987).

[25] Hopfield, J.J.: PNAS **79** 2554-2559 (1982).

[26] Huberman, B.A. and Hogg, T.: Physica **22D** 376–384 (1986).

[27] Bohr, H. and Brunak, S.: Complex Systems **3** 9–28 (1989).

[28] Honeycutt, J.D. and Thirumalai, D.: PNAS **87** 3526–3529 (1990).

[29] Wolfram, S.: Physica **22D** 385–399 (1986).

[30] Steinbach, P.J., Ansari, A., Berendzen, L., Braunstein, D., Chu, K., Cowen, B.R., Ehrenstein, D., Frauenfelder, H., Johnson, J.B., Lamb, D.C., Luck, S., Mourant, J.R., Nienhaus, G.U., Ormos, P., Philipp, R., Scholl, R., Xie, A., Young, R.D.: Biochemistry **30** 3988–4001 (1991).

[31] Yang, I.S. and Anderson, A.C.: Phys. Rev. **B34** 2942–29 (1986).

[32] Cannistraro, S., Giugliarelli, G., Marzola, P., Sacchetti, F.: Solid State Commun. **68** 369–373 (1988).

[33] Singh, G.P., Schink, H.J., Lohneysen, H.V., Parak, F., Hunklinger, S.: Z. Phys. **B55** 23–26 (1984).

[34] Drews, A.R., Thayer, B.D., Stapleton, H.J., Wagner, G.C., Giugliarelli, G., Cannistraro, S.: Biophys. J. **57** 157–162 (1990).

[35] Cannistraro, S.: J. Phys. (France) **51** 131–139 (1990).

[36] Doster, W., Bachleitner, A., Dunau, R., Hiebl, M., Luscher, E.: Biophys. J. **50** 213–219 (1986).

[37] Kohler, W., Friedrich, J., Scheer, H.: Phys.Rev. **A37** 660–662 (1988).

[38] Doster, W., Cusack, S., Petry W.: Phys. Rev.Lett. **65** 1080–1083 (1990).

[39] Doster, W., Cusack, S., Petry, W.: Nature **337** 754–756 (1989).

[40] Parak, F., Hartmann, H., Aumann, K.D., Reuscher, H., Rennekamp, G., Bartunik, H., Steigemann, W.: Eur. Bio. J. **15** 237–249 (1987).

[41] Kuczera, K., Kuriyan, J., Karplus, M.: J. Mol. Biol. **213** 351–373 (1990).

[42] Kendrew, J.C., Dickerson, R.E., Strandberg, B.E., Hart, R.G., Davies,

D.R., Phillips, D.C., Shore, V.C.: Nature **185** 422–427 (1960).

[43] Cantor, C.R. and Schimmel: "Biophysical Chemistry " Freeman Publications, San Francisco (1980).

[44] Braunstein, D., Ansari, A., Berendzen, J., Cowen, B.R., Egeberg, K.D., Frauenfelder, H., Hong, M.K., Ormos, P., Sauke, T.B., Scholl, R., Schulte, P.J., Sligar, S.G., Springer, B.A., Steinbach, P.J., Young, R.D.: PNAS **85** 8497–8501 (1988).

[45] Alberting, N., Austin, R.H., Chan, S.S., Eisenstein, L., Frauenfelder, H., Nordlund, T.M.: J. Chem. Phys. **65** 4701–4711 (1976).

[46] Agmon, N. and Hopfield, J.J.: J. Chem. Phys. . **79** 2042–2053 (1983).

[47] Young, R.D. and Bowne, S.F.: J. Chem. Phys. **81** 3730–3737 (1984).

[48] Srajer, V., Reinisch, L., Champion, P.M.: J. Am. Chem. Soc. **110** 6656–6670 (1988).

[49] Abragam, A. and Bleaney, B.:" Electron Paramagnetic Resonance of Transition Ions ", Clarendon Press, Oxford, (1970). *and refs. therein.*

[50] Pake, G.E.: "Paramagnetic Resonance: an introduction monograph", Benjamin, New York (1962).

[51] Kotani, M.: Adv. Quantum Chem. **4** 227–266 (1968).

[52] McGarvey, B.R.: "Electron Spin Resonance of Transition–Metal Complexes", ed. by Carlin, R.L., Marcel Dekker Inc. New York (1966).

[53] Tanabe, Y. and Sugano, S.: J. Phys. Soc. Japan **9** 87 (1954).

[54] Takano, T.: J. Mol. Biol. **110** 569–584 (1977).

[55] Gibson, J.F. : "EPR of iron in biological systems" (Bertini,I. and Drago, R.,S. eds.) pp.225–253, ESR and NMR of Paramagnetic Species in Biological and related Systems, D.Reider publishing Company (1979).

[56] Peisach, J., Blumberg, W.E., Ogawa, S., Rachmilewitz, E.A., Oltzik, R.:

J. Biol. Chem. **25** 3342–3355 (1971).

[57] Scholes, C.P.: J. Chem. Phys. **52** 4890–4895 (1970).

[58] Brill, A.S., Fiamingo, F.G., Hampton, D.A.: J. Inorg. Biochem. **28** 137–143 (1986).

[59] Fiamingo, F.G., Brill, A.S., Hampton, D.A., Thorkildsen, R.: Biophys. J. **55** 67–77 (1989).

[60] Pilbrow, J.R.: J. Magn. Resonance **58** 186–203 (1984).

[61] Cannistraro, S. and Giugliarelli, G.:. Mol. Phys. **58** 173– 179 (1986).

[62] Aasa, R. and Vanngard, T.: J. Magn. Resonance **19** 308–315 (1975).

[63] Isomoto, A., Watari, H., Kotani, M.: J. Phys. Soc. Japan **29** 1571–1577 (1970).

[64] Brill, A.S.: "Transition Metal in Biochemistry " Springer–Verlag, New York (1977).

[65] Hagen, W.R.: J. Magn. Resonance. **44** 447–469 (1981).

[66] Hagen, W.R., Hearshen, D.O., Sands, R.H., Dunham, W.R.: J.Magn. Res. **61** 220–232 (1985).

[67] Hagen, W.R., Hearshen, D.O., Harding, L.J., Dunham, W.R.: J. Magn. Res. **61** 233–244 (1985).

[68] More, C., Bertrand, P., Gayda, J.P.: J. Magn. Resonance **73** 13–22 (1987).

[69] Yang, A.S. and Gaffney, B.J.: Biophys. J. **51** 55–67 (1987).

[70] Giugliarelli, G. and Cannistraro, S.: Il Nuovo Cimento **4** 194–205 (1984).

[71] Kirkpatrick, S., Gelatt, C.D., Vecchi, M.P.: Science **220** 671–680 (1983).

[72] Press, W.H., Flannery, B.P., Teukolsky, S. A., Vetterling, W.T.: "Numerical Recipes", pag. 274, Cambridge University Press, New York (1986).

[73] Riggs, A.: Methods Enzymol. **76** 5–9 (1981).

[74] Giugliarelli, G., Tancini, P., Cannistraro, S.: J. Phys. E (Sci. Instrum.)

22 702–708 (1989).

[75] Brill, A.S., Fiamingo, F.G., Hampton, D.A., Levin, P.D., Thorkildsen, R.: Phys. Rev. Lett. **54** 1864–1867 (1985).

[76] Bizzarri, A.R. and Cannistraro, S.: submitted to Appl. Magn. Res.

[77] Hori, H., Iketa–Saito, M., Yoketani, T.: Nature **288** 501–501 (1980).

[78] Ondrias, M.R., Rousseau, D.L.: Science **213** 657–659 (1981).

[79] Ollis, D.L., Writht, P.E., Pope, J.M., Appleby, C.A.: Biochemistry **20** 587–593 (1981).

[80] Stryer, L.: Biochemistry, 3rd ed. New York: Freedman and Company (1988).

[81] Schäffer, C.E. and Jorgensen, C.K.: Mol. Phys. **9** 401–410 (1965).

[82] Burdett, J.K. : "Molecular Shapes– Theoretical Models of Inorganic Stereochemistry", Wiley and Sons, New York (1980).

[83] Wolfsberg, M. and Helmholtz, L.: J. Chem. Phys. **20** 837–846 (1952).

[84] Bacci, M.: Chem. Phys. **40** 237–244 (1979).

[85] Takano, T.: J. Mol. Biol. **110** 537–568 (1977).

[86] Bacci, M.: Biophys. Chem. **11** 39–47 (1980).

[87] Evans, S.V. and Brayer, G.D.: J. Mol. Biol. **213** 885–897 (1990).

[88] Parak, F. and Knapp. E.W.:PNAS **81** 7088–7092 (1984).

[89] Nadler, W., Brunger, A.T., Schulten, K., Karplus, M.: PNAS **84** 7933–7937 (1987).

[90] Gerloch, M. and Slade, R.C.:" Ligand–field parameters" Cambridge University Press, Cambridge (1973).

[91] Buhks, E. and Jortner, J.: J. Chem. Phys. **83** 4456–4462 (1985).

[92] McCammon, J.A., Wolynes, P.G., Karplus, M.: Rep. Prog. Phys. **47** 1–46 (1984).

[93] Singh, G.P., Parak, F., Hunklinger, S., Dransfeld, K.: Phys. Rev. Lett. **47** 685–688 (1981).

[94] Gekko, K., Timasheff, S.N.: Biochemistry **20** 4667–4676 (1981).

[95] Gerlma, S.Y.: Eur. J. Biochem. **14** 150–156 (1970).

[96] Timasheff, S.N., Lee, J.C., Pittz, E.P., Tweedy, N.: J. Colloid. Interfac. Sci. **55** 658–663 (1976).

[97] Lee, J.C. and Timasheff, S.N.: J. Biol. Chem.. **251** 523–532 (1981).

Acknowledgements

I would like to thank Prof. Antonio Borsellino for introducing me to Biophysics and for giving me the opportunity to work in the Biophysical Sector. I would like to thank Dr. Mauro Bacci for valuable suggestions and for his help in developing of the AOM programs. Thanks are also due to Dr. Raffaele Lamanna for his friendly support and for helpful discussions. Finally, I wish to thank the Director and the staff of the INFN (sez. Perugia) for providing computer facilities.